The Astrophysical Journal, 926:186 (20pp), 2022 February 20 https://doi.org/10.3847/1538-4357/ac3a89

GASKAP Pilot Survey Science. II. ASKAP Zoom Observations of Galactic 21 cm Absorption

John M. Dickey[1], J. M. Dempsey[2,3], N. M. Pingel[2], N. M. McClure-Griffiths[2], K. Jameson[4], J. R. Dawson[5,6], H. Dénes[7], S. E. Clark[8,9], G. Joncas[10], D. Leahy[11], Min-Young Lee[12], M.-A. Miville-Deschênes[13], S. Stanimirović[14], C. D. Tremblay[15], and J. Th. van Loon[16]

[1] School of Natural Sciences, Private Bag 37, University of Tasmania, Hobart, TAS, 7001, Australia
[2] Research School of Astronomy & Astrophysics, Australian National University, Canberra, 2611, Australia
[3] CSIRO Information Management and Technology, GPO Box 1700, Canberra, ACT 2601, Australia
[4] Bolton Fellow, CSIRO Space and Astronomy, 26 Dick Perry Avenue, Kensington, WA 6151, Australia
[5] Department of Physics and Astronomy and MQ Research Centre in Astronomy, Astrophysics and Astrophotonics, Macquarie University, NSW 2109, Australia
[6] CSIRO Space and Astronomy, Australia Telescope National Facility, PO Box 76, Epping, NSW 1710, Australia
[7] ASTRON, The Netherlands Institute for Radio Astronomy, Oude Hoogeveensedijk 4, 7991 PD, Dwingeloo, The Netherlands
[8] Department of Physics, Stanford University, Stanford, CA 94305-4060, USA
[9] Kavli Institute for Particle Astrophysics & Cosmology (KIPAC), Stanford University, Stanford, CA 94305, USA
[10] Département de Physique, de Génie Physique et d'Optique, Université Laval, Québec, G1V 0A6, Canada
[11] Department of Physics and Astronomy, University of Calgary, Calgary, AB T2N 1N4, Canada
[12] Korea Astronomy and Space Science Institute, 776 Daedeokdae-ro, 34055, Daejeon, Republic of Korea
[13] Laboratoire AIM, CEA/CNRS/Université Paris-Saclay, F-91191 Gif-sur-Yvette, France
[14] Department of Astronomy, University of Wisconsin, Madison, WI 53706, USA
[15] CSIRO Space and Astronomy, Australia Telescope National Facility, PO Box 1130, Bentley, WA 6102, Australia
[16] Lennard-Jones Laboratories, Keele University, ST5 5BG, UK

Received 2021 September 30; revised 2021 November 6; accepted 2021 November 15; published 2022 February 23

Abstract

Using the Australian Square Kilometre Array Pathfinder to measure 21 cm absorption spectra toward continuum background sources, we study the cool phase of the neutral atomic gas in the far outer disk, and in the inner Galaxy near the end of the Galactic bar at longitude 340°. In the inner Galaxy, the cool atomic gas has a smaller scale height than in the solar neighborhood, similar to the molecular gas and the super-thin stellar population in the bar. In the outer Galaxy, the cool atomic gas is mixed with the warm, neutral medium, with the cool fraction staying roughly constant with the Galactic radius. The ratio of the emission brightness temperature to the absorption, i.e., $1 - e^{-\tau}$, is roughly constant for velocities corresponding to Galactic radius greater than about twice the solar circle radius. The ratio has a value of about 300 K, but this does not correspond to a physical temperature in the gas. If the gas causing the absorption has kinetic temperature of about 100 K, as in the solar neighborhood, then the value 300 K indicates that the fraction of the gas mass in this phase is one-third of the total H I mass.

Unified Astronomy Thesaurus concepts: Diffuse interstellar clouds (380); Intercloud medium (803); Interstellar absorption (831); Interstellar atomic gas (833); Interstellar phases (850)

1. Background

A galaxy's lifeblood is its interstellar medium (ISM). A spiral galaxy evolves through the cycle of star formation and stellar mass loss leading to gradually increasing gas-phase metallicity. Physical conditions in the ISM cover the full range between the coldest molecular clouds, with temperatures $T \simeq 10$ K, to the fully ionized interiors of supernova remnant-blown bubbles and chimneys with $T > 10^6$ K. The atomic hydrogen (H I) populates regions of intermediate density and temperature, primarily in two phases, the cool neutral medium (CNM) with temperatures between 20 and 150 K and the warm neutral medium (WNM) with temperatures between about 6000 and 10,000 K (Kulkarni & Heiles 1987; Ferrière 2001). Deep surveys of 21 cm absorption with the Very Large Array telescope show that there is a population of atomic clouds with intermediate temperatures, from a few hundred to a few thousand Kelvins, called the unstable neutral medium (UNM; Murray et al. 2015) because it is thermally unstable in the classic two-phase theory of Field et al. (1969). As the more abundant phase, the WNM dominates 21 cm emission spectra, but in 21 cm absorption, the WNM disappears, and only the CNM is visible, with low-level traces of the UNM, which explains the dramatic difference in shape between the Galactic 21 cm emission and the absorption spectra (Clark 1965; Murray et al. 2021). In spiral galaxy disks, conditions allow heating-cooling equilibrium for both the WNM and CNM at a range of typical ISM pressures; thus both phases coexist inside and outside the solar circle (Wolfire et al. 2003; Bialy & Sternberg 2019). The CNM is more difficult to image than the WNM, because sensitive absorption spectra require bright continuum background sources, but to understand the thermal balance, and the interaction between the gas and the radiation field more generally, we need to study the CNM along with the WNM, i.e., the 21 cm absorption along with the emission.

To maintain the star formation rate observed in the Milky Way (MW) and other spiral galaxies, and to understand the abundance of metals and their recycling, the circumgalactic medium (CGM) is indispensable (Putman et al. 2012; Tumlinson et al. 2017). Although the gas halo outside the MW disk is mostly warm to very hot and highly ionized (Miller & Bregman 2015), it can coexist with atomic hydrogen structures like the Magellanic Stream (Fox et al. 2014). At the

outer edges of the MW disk, with galactocentric radius R in the range 30 to 40 kpc (Kalberla & Dedes 2008), the disk and halo must have an interface. This may be the region where the cold-mode accretion from the CGM to the ISM is underway (Bland-Hawthorn et al. 2017)

Surveys of the 21 cm line in emission show the structure and rotation of the H I gas in the MW disk and halo (Kalberla & Kerp 2009). The thermal velocity of the WNM smooths emission spectra so that lines are typically ∼10 km s^{-1} wide. In absorption, CNM features are typically much narrower than in emission. When it is possible to translate absorption velocities to distances, the narrower lines provide better distance resolution. The filling factor of the CNM is lower than the WNM by an order of magnitude (Dickey & Lockman 1990; ∼5% and ∼50% respectively); absorption picks out the dense regions. For these reasons, we can sometimes get a better resolution of the Galactic structure with the CNM than with the WNM, e.g., small offsets of the H I disk from the Galactic midplane.

The molecular clouds, type II supernovae, and synchrotron emissivity all drop off with R following an exponential distribution with scale length similar to that of most stellar populations, typically 2.0–3.9 kpc (Bland-Hawthorn & Gerhard 2016; Miville-Deschênes et al. 2017; Chrobáková et al. 2020). But the WNM has a much larger radial extent. For $R < \sim 12$ kpc, the surface density of H I, Σ, is roughly flat based on 21 cm emission surveys (Kalberla & Dedes 2008); beyond 12 kpc, Σ drops exponentially with scale length 3.75 kpc, to $R \sim 35$ kpc. Beyond 35 kpc, the radial scale length increases, the disk disappears, and the trace H I remaining is distributed in a halo. Since the CNM phase is intermediate between the WNM and the molecular clouds, its radial variation might follow that of the molecular emission or that of the H I emission, or something in between. Although the sampling was sparse, surveys of absorption that were available 15 yr ago indicated that the CNM has the same radial distribution as the WNM, i.e., the phase mixture is constant with the radius (Dickey et al. 2009). That result came as a surprise, because at the very low pressures in the outer disk, the heating-cooling equilibrium curve favors the WNM, with a minimum pressure below which the CNM cannot exist at all (Wolfire et al. 2003; Bialy & Sternberg 2019). The need for a better understanding of the phase mixture in the outer MW disk motivates further observations, particularly in the fourth quadrant where the Galactic warp does not cause the outer disk to depart significantly from latitude $b = 0°$.

The recently commissioned Australian Square Kilometre Array Pathfinder (ASKAP) is a powerful survey instrument, described by Hotan et al. (2021). The telescope is built around a revolutionary phased-array-feed (PAF) technology (Chippendale et al. 2010, 2016). With 36 antennas, ASKAP has a huge number of short baselines (<1 km) that give it the superior brightness sensitivity that is crucial for Galactic and extragalactic 21 cm emission mapping, and it has a large number of longer baselines, out to 6 km, that allow a synthesized beam size smaller than 10″. This resolution is optimal for extragalactic continuum source counts, and it is just what is needed for Galactic 21 cm absorption observations, where the line emission must be resolved out by the spatial high-pass filter obtained by using only the longer baselines.

In this paper, we consider 21 cm absorption in a single GASKAP pilot field centered at $(\ell, b) = (340°, 0°)$ that covers an area of ∼25 square degrees with resolution 10″. Imaging a spectral cube of such immense proportions is an intricate and long process (Pingel et al. 2022), but the absorption spectra used in this paper can be obtained more quickly with a separate processing pipeline (Dempsey et al. 2021). The observations and spectra are described in Section 2. The inner Galaxy velocity range (negative velocities at this longitude) is rich in absorption lines. In Section 3, we discuss absorption spectral averages near the terminal velocity, corresponding to the subcentral point where the line of sight (LoS) passes close to the far end of the MW bar and the 3 kpc arm. In Section 4, we study the CNM in the outer disk, outside the solar circle on the far side of the Galactic center. There are many distinct absorption lines that are detected in weighted averages of the spectra, with kinematic distances out to $R \sim 40$ kpc. We divide the GASKAP field into six subfields and make weighted averages of the spectra in each area. Averaging spectra over the entire area, we find little radial variation of the ratio of emission to absorption. Thus the ratio of WNM and CNM mass densities is roughly constant for $12 < R < 40$ kpc. Section 5 discusses the results in the context of cold-mode accretion and conditions in the outer disk, with focus on the potential applications of the full GASKAP survey of the Galactic plane that will begin in 2022.

2. Observations

The observations were taken as part of the Pilot phase 1 survey science program on ASKAP on 2020 April 26 and 27 with total integration time of 16 hr (SBID 13531 and 13536). The visibilities were calibrated with the standard ASKAPsoft (Guzman et al. 2019, version 1.0.14) and ASKAP pipeline (version 1.0.15.1) steps. The spectrometer used frequency zoom mode 5, which has channel spacing 1.1574 kHz over a total bandwidth of 18 MHz. For the spectra used here, there are 604 channels averaged to 1.0 km s^{-1} spacing and bandwidth, running from −268 to +335 km s^{-1} in the LSRK system (Gordon 1976). As described by Dempsey et al. (2020, 2021), the spectra are extracted from small cubes covering just 50″ × 50″ centered on positions of continuum sources selected by the SELAVY program (Whiting & Humphreys 2012) that is part of the ASKAP pipeline.

For Galactic 21 cm absorption studies, the limiting factor has long been confusion due to small-scale variations in the 21 cm line emission that make it impossible to accurately interpolate the emission toward the continuum source. To eliminate this source of noise, we high-pass filter the spatial frequencies of the images by deleting all the data from baselines shorter than 1.5 kλ = 317 m. The clean beam size is 7″.7 by 6″.2 (position angle −89°). The resulting cubes include only continuum and line emission with spatial scales significantly smaller than 3′. This effectively removes all vestiges of the Galactic 21 cm line in emission, except in some high-velocity clouds where the emission has an extremely small-scale angular structure. The extended continuum brightness is also filtered out by this process, leaving only the point sources, and whatever fraction of the extended sources may be concentrated on sizes smaller than about 20″.

The noise in the absorption spectra is due to the system temperature of the telescopes, primarily receiver noise, plus the sky brightness, which is dominated by the H I emission line as seen by the individual dishes in the telescope array. We compute this by smoothing the Parkes Galactic All Sky Survey (McClure-Griffiths et al. 2009) to the 62′ beam size of the

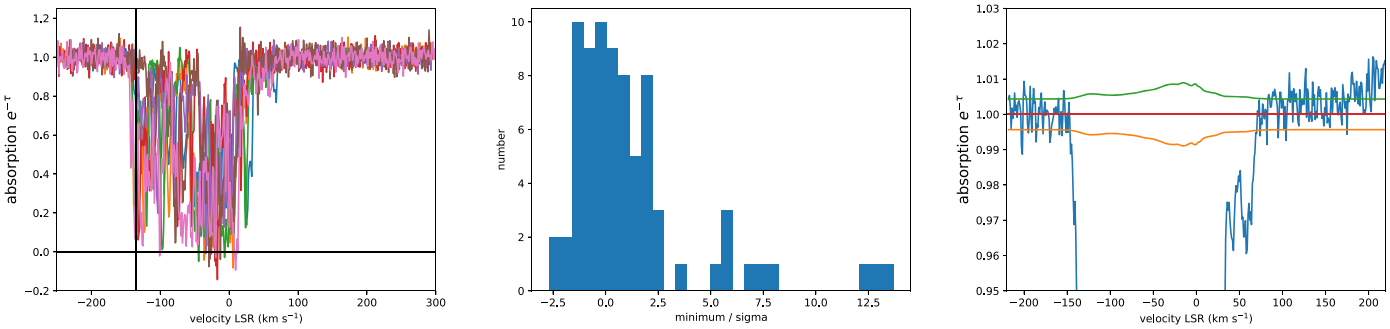

Figure 1. Sample spectra and spectrum averages. The left panel shows a superposition of seven extragalactic spectra at low latitudes ($|b| < 0°.5$). In all cases, the absorption spectra go close to zero at some velocities where the optical depth is very high. Most of the spectra go below zero, which is unphysical and often indicates problems with calibration of the bandpass shape or differences in processing of the continuum and spectral line channels. The center panel scales this overshoot by the rms noise in $e^{-\tau}$. The histogram shows the number of spectra vs. the ratio of the minimum value of $e^{-\tau}$ divided by σ_τ, for a sample of 77 extragalactic sources. The histogram shows that the spectra overshoot by up to ∼2.5 times the rms noise (σ_τ), but mostly by about $1\sigma_\tau$. A few spectra at higher latitudes ($|b| \sim 3°$) have no deep absorption lines, but most have at least one line that is nearly saturated ($\tau \to \infty$). The right-hand panel shows an average of the 77 spectra, with the scale expanded around $\tau = 0$ showing that the spectral baselines are very flat. Some curvature is noticeable at velocities v > 180 km s^{-1}. The noise envelope broadens at velocities where the 21 cm emission has increased the system temperature of the receivers.

ASKAP dishes centered on the position of each beam formed from the PAF outputs. Thus the noise is a function of velocity across the spectra, typically increasing up to a factor of two compared to its off-line value.

The 21 cm emission cubes come from a very different and more involved processing pipeline, described by Pingel et al. (2022), that includes joint deconvolution of all the fields together, followed by the delicately calibrated combination of single dish H I survey data from Parkes (McClure-Griffiths et al. 2009). As this emission processing is ongoing, we concentrate in this paper on the results from the absorption spectra, with comparison to the Parkes single dish data taken from the HI4PI distribution (HI4PI Collaboration et al. 2016).

Some sample absorption spectra are shown in Figure 1. The bandpass calibration is so precise that there was no need for baseline fitting; the off-line channels give a very flat baseline at $e^{-\tau} = 1$ precisely. The deepest lines show the intensity going to zero, but not beyond zero by more than ∼2 times the rms noise. This confirms that the continuum and spectral channels have no relative calibration offsets. Spectral line surveys can have optical depth scale problems if the continuum is subtracted from the data as part of the mapping process. This can cause drastic errors in τ at high optical depths where the continuum is absorbed to almost zero.

2.1. Galactic versus Extragalactic Background Sources

The SELAVY tool used for continuum source-finding is powerful, but the results need to be checked. In this field, there are many extended sources that are heavily resolved by the telescope and filtered into a few high points by the UV minimum. SELAVY catalogs these as separate sources, but by inspection and comparison with lower-resolution continuum maps (e.g., Haverkorn et al. 2006), we group together sources that are blended by the beam, or are clearly part of a single, larger continuum structure. Many extragalactic sources are doubles. These we leave as a single source if the two components are blended by the beam, i.e., within about 15″; if they are distinct points, we treat them as separate background sources. After removing duplicates, there are 295 distinct sources, whose positions are determined by Gaussian fitting. The source positions are listed in the Appendix.

The density of spectra per square degree in this survey (8.2) is higher than in the Southern Galactic Plane Survey (SGPS; McClure-Griffiths et al. 2005) by a factor of six, and orders of magnitude higher than in any other 21 cm absorption survey in the fourth quadrant. This high density of background sources makes it possible to trace the distribution of CNM in the absorbing clouds, and to measure the covering factor of absorption, i.e., the chance of a LoS not showing absorption at velocities where strong absorption is seen on nearby sightlines. But this analysis depends on separating the continuum sources into two groups, Galactic and extragalactic.

Source identifications were made by matching catalogs from VizieR[17] using maximum separation 36″: from catalogs of supernova remnants (Green 2019, 6 matches), submillimeter compact sources from ATLASGAL (Urquhart et al. 2014, 86 matches), H II regions selected from the WISE survey (Anderson et al. 2015, 80 matches), 14 young stellar objects (YSO), plus three planetary nebulae (Riggi et al. 2021; Preite-Martinez 1988), one pulsar (Manchester et al. 2005),[18] and two sources on the rim of the S36 bubble (Churchwell et al. 2006). After this matching, we find 105 of the 295 continuum sources are Galactic; the other 190 are assumed to be extragalactic. Figure 2 shows the source positions and the latitude distributions of the Galactic and extragalactic sources.

Many of the sources show interesting structure; in particular arcs or shells of continuum are apparent in several Galactic sources. Because of the high-pass filtering, absolute flux density values are not useful for comparison with other surveys, and they are not tabulated. The index numbers on the tables in the Appendix are based on the original SELAVY list of 347 sources; thus there are many gaps in the sequence.

2.2. Comparison with the Southern Galactic Plane Survey

The field observed here was covered in the SGPS. The strongest, most compact continuum sources were studied for absorption in the 21 cm line by Strasser (2006). The rms noise was typically three to ten times larger than in the GASKAP spectra, and there is confusion due to residual emission fluctuations. Some comparisons are shown in Figure 3. The spectra are generally consistent to within the noise, but the SGPS spectra show occasional spurious positive and negative fluctuations at extreme negative and positive velocities,

[17] https://vizier.u-strasbg.fr/viz-bin/VizieR
[18] https://www.atnf.csiro.au/research/pulsar/psrcat v. 1.64.

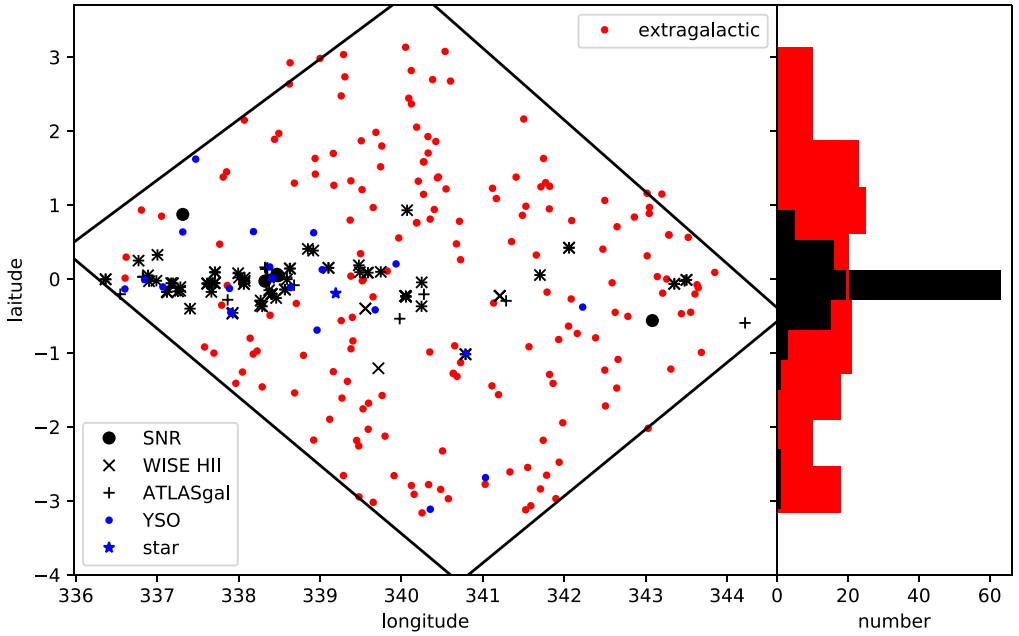

Figure 2. The distribution of continuum sources in the GASKAP field. On the left is a map of the field showing all sources, extragalactic in red and Galactic in black and blue, with different symbols for different types. The right panel shows histograms of the latitude distribution of the Galactic and extragalactic sources. Since the longitude range decreases with $|b|$, there are fewer extragalactic sources at high latitudes. The edges of the field are scalloped by the beam forming step, but the four black lines show roughly the extent of the PAF footprint.

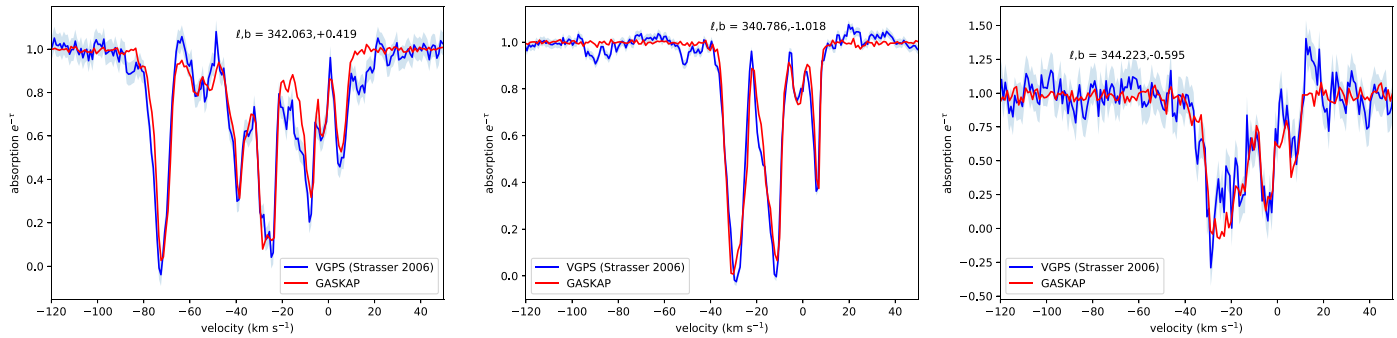

Figure 3. Comparison with spectra from the SGPS (Strasser 2006). The blue shading indicates the 1σ noise level in the SGPS data, which is typically larger than that of the GASKAP spectra by a factor of three to ten. The left and center panels are spectra toward bright continuum sources, so that discrepancies between the two surveys are due to emission fluctuations causing confusion that manifests as positive or negative *pseudo-absorption* (Radhakrishnan et al. 1972). The right-hand panel shows spectra toward a weaker continuum source, so the radiometer noise dominates at most velocities, but some discrepancies above the noise are apparent.

corresponding to the more distant gas, that are not present in the GASKAP data. The zero-point ($\tau \to \infty$) is also much better defined in the GASKAP spectra (Figure 1).

3. H I near the Terminal Velocity

Longitude 340° was chosen for the first GASKAP pilot field at $b = 0°$ because this LoS samples some of the most important features in the inner and outer disk, including the 3 kpc arm and the far end of the long bar, as well as the Scutum-Centaurus Arm both inside and again outside the solar circle. Figure 4 shows the Galactic structure visible through this small *keyhole* opened by the ∼5° square PAF field of view. In the fourth quadrant, Doppler shifts due to differential rotation give negative velocities inside the solar circle, reaching to the terminal velocity at the subcentral or tangent point, where the LoS comes closest to the Galactic center. At longitude 340°, the subcentral point is in the middle of the 3 kpc Arm, an anomalous structure that shows a Galactocentric radial velocity of about 50 km s^{-1} at longitude 0°. At the subcentral point, the Galactic radial velocity is perpendicular to the LoS, so it does not affect the Doppler shift.

The GASKAP spectra are rich with absorption features at negative velocities, corresponding to CNM structures in the inner Galaxy. Particularly prominent is the line at $v_{\rm LSR} \simeq -30$ km s^{-1} (Figure 3 middle and right panels) that is due to cold clouds in the Scutum-Centaurus Arm at distance $d \sim 2.8$ kpc and Galactocentric radius $R \simeq 5.8$ kpc, (using kinematic distances from Wenger et al. 2018; Reid & Menten 2019; based on $R_o = 8.31$ kpc and $\Theta_o = 240$ km s^{-1}). Of particular interest is the gas near the subcentral point, at a distance $d \sim 7.7$ kpc and velocity of about -135 km s^{-1}. The terminal velocity versus longitude in the fourth quadrant has been shown to follow a nearly linear trend with $\sin\ell$:

$$v_{\rm term}(\ell) = -177.7 \cdot (1 - |\sin(\ell)|) - 18.4 \text{ km s}^{-1} \quad (1)$$

(McClure-Griffiths & Dickey 2016). In the analysis shown in Figure 5, we offset each absorption spectrum by the difference between $v_{\rm term}(\ell)$ and -135 km s^{-1} so that a given velocity

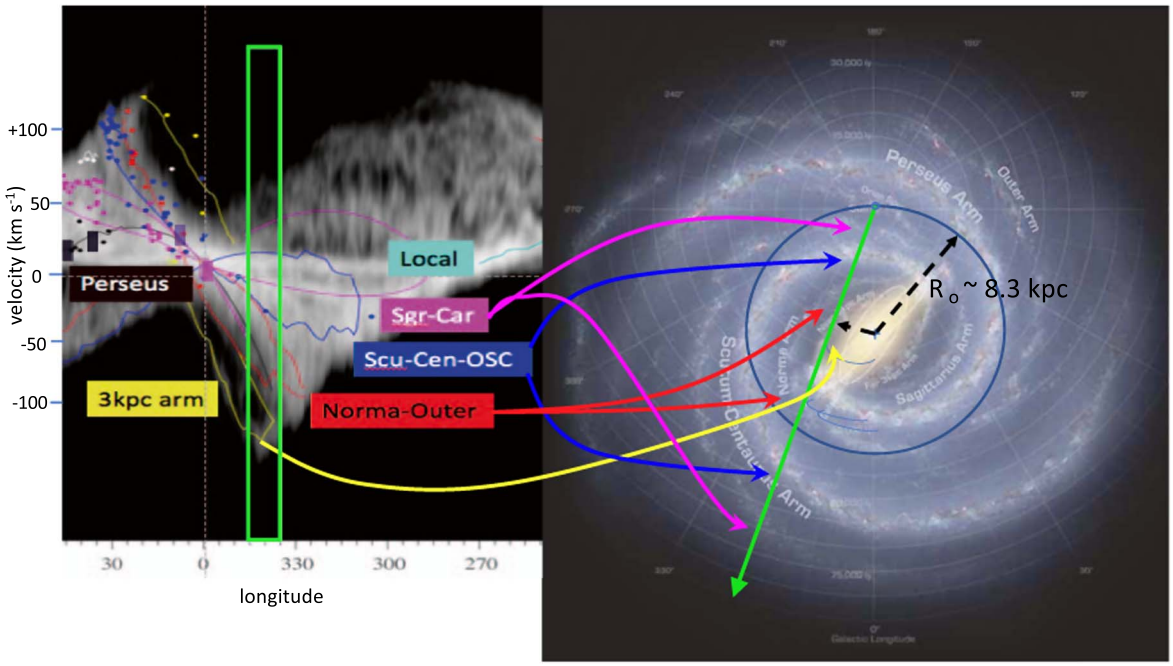

Figure 4. Two views of the GASKAP Pilot field. The left panel is a longitude–velocity diagram of 21 cm emission taken from Reid & Menten (2019, Figure 3), with gray scale showing the LAB survey emission (Kalberla et al. 2005), and colored curves tracing spiral arms based on VLBI parallax distances to masers in star formation regions. The white rectangle shows the longitude coverage of the GASKAP field. The right panel is the familiar Hurt/Benjamin/Churchwell figure (Churchwell et al. 2009) with the superposed line of sight (LoS) at 340° longitude in green. Note that this LoS has tangent point in the midst of the 3 kpc arm, it passes close to the far end of the Galactic bar (the *long bar*; e.g., Benjamin 2008; Wegg et al. 2015), and outside the solar circle, it passes through the Scutum-Centaurus Arm at velocity roughly +5 km s^{-1}, then farther out the Sagittarius-Carina Arm, at about +25 km s^{-1}. At larger Galactic radii, the more distant features in the l-v diagram are controversial, connecting either with the Perseus Arm and/or the Norma Arm and/or the Scutum-Outer Arm (e.g., Koo et al. 2017; Vallée 2020), depending on the pitch angles.

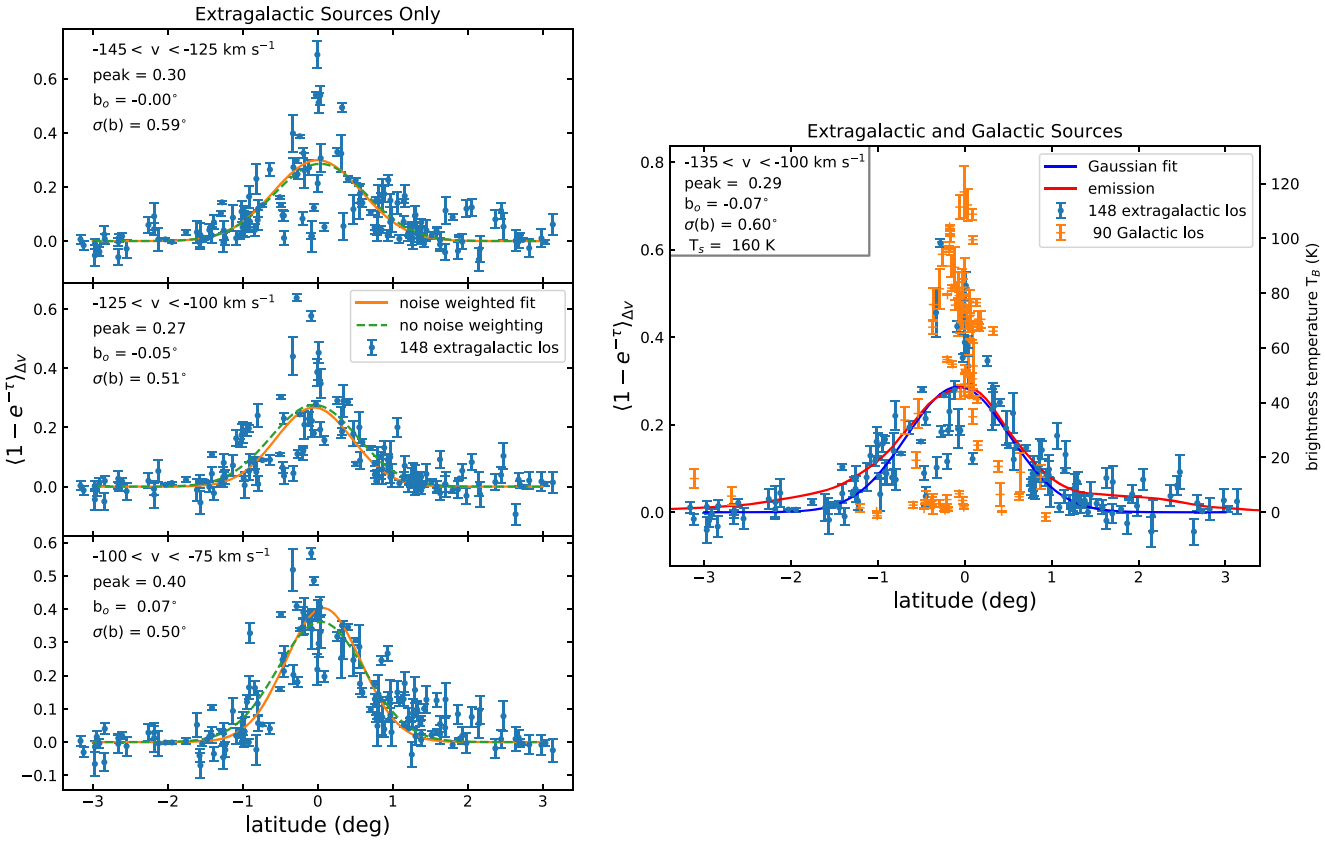

Figure 5. Mean absorption vs. latitude near the terminal velocity. The left panel shows absorption, $\langle 1 - e^{-\tau} \rangle$ (Equation (2)), toward extragalactic sources only. The right panel includes the Galactic source spectra, which show much larger scatter, and the emission brightness temperature.

Table 1
Gaussian Fits to Absorption versus Latitude near the Terminal Velocity

Velocity Range km s^{-1}	Weighted Fit Peak $1-e^{-\tau}$	Weighted Fit b Center deg	Weighted Fit σ_b Width deg	T_s K	Unweighted Fit Peak $1-e^{-\tau}$	Unweighted Fit b Center deg	Unweighted Fit σ_b Width deg
$-145 < v < -125$	0.30 ± 0.02	0.0 ± 0.04	0.59 ± 0.03		0.29 ± 0.02	$+0.03 \pm 0.05$	0.62 ± 0.04
$-125 < v < -100$	0.27 ± 0.02	-0.05 ± 0.03	0.51 ± 0.03		0.28 ± 0.02	-0.05 ± 0.04	0.58 ± 0.04
$-100 < v < -75$	0.40 ± 0.02	$+0.07 \pm 0.02$	0.50 ± 0.02		0.36 ± 0.02	$+0.04 \pm 0.03$	0.58 ± 0.03
$-135 < v < -100$	0.29 ± 0.01	-0.07 ± 0.03	0.60 ± 0.02	160	0.30 ± 0.01	-0.04 ± 0.03	0.61 ± 0.03
$0 < v < +8$	0.37 ± 0.03	$+0.11 \pm 0.05$	0.59 ± 0.05	123	0.37 ± 0.03	$+0.08 \pm 0.05$	0.47 ± 0.06
$1-e^{-\tau}$ baseline	0.34 ± 0.02				0.37 ± 0.02		
$+15 < v < +30$	0.39 ± 0.02	-0.62 ± 0.03	0.60 ± 0.03	176	0.42 ± 0.02	-0.76 ± 0.03	0.63 ± 0.04
$+45 < v < +65$	0.05 ± 0.01	-0.27 ± 0.052	1.20 ± 0.06	325	0.05 ± 0.01	-0.15 ± 0.20	1.43 ± 0.25
Two-phase Emission Fit							
		CNM		T_{CNM}		WNM	
$-135 < v < -100$	35 K	-0.074	0.596	121 K	11 K	$+0.1$	1.6

interval near -135 km s^{-1} will include the same line-of-sight interval near the subcentral point.

In Figure 5, the left panel shows the mean absorption, as a function of latitude, where the mean absorption is defined as:

$$\langle 1 - e^{-\tau} \rangle_{\Delta v} = 1 - \frac{\int_{\Delta v} e^{-\tau}\, dv}{\Delta v}, \quad (2)$$

i.e., one minus the equivalent width computed over a chosen velocity interval, Δv, divided by the velocity interval. Three different velocity intervals near the terminal velocity are shown on the three panels. For the upper panel on the left of Figure 5, the velocity range, Δv, is [-145,-125] km s^{-1}, which straddles the nominal terminal velocity (-135 km s^{-1} at $\ell = 340°$) and thus is dominated by the 3 kpc Arm near the subcentral point. The middle and lower panels step back in velocity from the terminal velocity, and thus correspond to two regions along the LoS offset on either side of the subcentral point, with Δv edges at $v = -100$ km s^{-1} ($R = 3.6$ kpc) and $v = -75$ km s^{-1} ($R = 4.1$ kpc). The blue points are the values for each of the 151 brightest extragalactic background sources that give the most sensitive absorption spectra, having off-line rms noise $\sigma_\tau < 0.3$. Each point is weighted by σ_τ^{-2} in the fitting (using scipy.optimize routine curve_fit) to fit the Gaussians shown as the solid curves in Figure 5. We also compute the unweighted best-fit Gaussians, i.e., weighting each point equally, shown as the dashed curves. The resulting fit parameters for each velocity range are shown on the figures, and tabulated on Table 1.

The right panel of Figure 5 shows a similar fit to the absorption toward the extragalactic sources, averaged over a broader range, $\Delta v = [-135, -100]$ km s^{-1}, with points for the Galactic sources added to show the much larger scatter in absorption at the terminal velocity for this sample. On the right panel, the 21 cm emission brightness temperature, T_b, is the average of HI4PI spectra over the field area, integrated over the same velocity range as for the absorption points. The T_b scale on the right-hand axis is chosen so that the two curves peak at the same height; there is a factor of 158 between the two scales.

Table 2
Scale Height of the Absorbing Layer

Δ_v km s^{-1}	v_o km s^{-1}	R kpc	d_1 kpc	d_2 kpc	σ_b	σ_{z1} pc	σ_{z2} pc
[−145, −125]	−135	2.8	7.8	...	0°.59	80	...
[−125, −100]	−112.5	3.0	6.5	9.3	0°.51	58	83
[−100, −75]	−87.5	3.7	5.5	10.3	0°.50	48	90
[0, +8]	+4	8.3	15.6	...	0°.59	160	...
[+15, +30]	+22.5	12.5	20	...	0°.60	210	...
[+45, +65]	+55	32	33	...	1°.2	690	...

The value of σ_b in the Gaussian fits in Figure 5 and Table 1 is particularly interesting; this gives an estimate for the scale height (σ_z) of the CNM given the distance corresponding to the velocity interval, Δv. These scale heights are given on Table 2. At the terminal velocity the distance is unique, while, at the stepped-back velocity ranges of the lower panels in Figure 5, the two kinematic distances diverge, d_1 and d_2 on columns 4 and 5 (Wenger et al. 2018). These give two values for the scale height, σ_z (columns 7 and 8). In general the results for σ_z are in the range 50 to 90 pc in the inner Galaxy.

These values for σ_z, the scale height of the cool gas layer, are considerably smaller than the estimate for the solar neighborhood, ∼125 pc (Lockman 1984; Lockman & Gehman 1991; Malhotra 1995; Ferrière 2001; Su et al. 2021), but this variation is to be expected given the gravitational effect of the super-thin stellar component in the bar, with scale height of just 45 pc, determined by Wegg et al. (2015). When a larger sample of absorption spectra is available from the full GASKAP survey, the improved precision will allow precision mapping of the scale height, warp and corrugations of the midplane, and ultimately the filling factor of the CNM clouds as functions of R.

The right-hand panel of Figure 5 includes the mean absorption in the adjusted velocity range $-135 < v < -100$ km s^{-1} for the Galactic sources. In this case, there are many Galactic LoS that show no absorption at all in this velocity interval, even though they are mostly all near latitude $b = 0°$. These are probably more nearby than the subcentral point.

There is a second group that shows about the same absorption as the extragalactic sources, $(1-e^{-\tau}) \simeq 0.3$, and a third group that shows much more absorption than most of the extragalactic sources, from 0.4 to 0.65. The latter group may correspond to continuum sources near the end of the Galactic bar, where there is active star formation and molecular gas. The high optical depths would then be due to the cold H I surrounding or mixed with the star-forming clouds.

At the highest velocities (-125 to -145 km s^{-1}, top left panel of Figure 5), the extragalactic absorption points resemble the Galactic sources on the right-hand panel; the scatter around the fitted Gaussian is large, and there are some points near latitude zero that show very little absorption; the mean of $(1-e^{-\tau})$ over this velocity range is below 0.1. This suggests that absorption within 10 km s^{-1} of the terminal velocity is spotty, sometimes there are CNM clouds very near the subcentral point, and sometimes not. So the CNM is not a solid curtain; it has gaps that leave some LoS unabsorbed. This should be kept in mind when assigning near-far kinematic distances based on the presence or absence of absorption at the terminal velocity. When the absorption is present it is a good indicator of the far side distance, but when absorption is not seen in the last 10 km s^{-1} before the terminal velocity, this does not prove that the source is at the near distance. Averaging the absorption spectrum over 25 km s^{-1} or more back from the terminal velocity, as in the lower two panels on the left of Figure 5, is more conclusive.

3.1. Comparison with Emission

Measuring the excitation temperature of the 21 cm line transition, i.e., the *spin temperature*, requires combination of emission and absorption spectra. The simplest, one-phase assumption gives

$$T_s = \frac{T_b}{1 - e^{-\tau}} \tag{3}$$

where T_b is the brightness temperature of the 21 cm emission corresponding to the absorption, $e^{-\tau}$ (Draine 2011, Section 8.2). Hereafter we will call T_s the mean spin temperature, because it generally represents an average of a mixture of different gas temperatures at the same velocity along the LoS. Since the spin temperature has a very wide range, from about 20 to 10^4 K (e.g., Murray et al. 2015, 2018), values derived from Equation (3) can be quite different from either the CNM or WNM temperatures. If two regions, 1 and 2, with low optical depths and different spin temperatures, overlap in radial velocity, then the measured value of T_s is the harmonic mean:

$$T_s = \frac{N_1 + N_2}{\left(\frac{N_1}{T_1}\right) + \left(\frac{N_2}{T_2}\right)} \quad (\tau_1, \tau_2 \ll 1) \tag{4}$$

where the column density, N, is the velocity integral of the emission brightness temperature spectrum, T_b, by

$$\frac{N}{\mathrm{cm}^{-2}} = 1.82 \cdot 10^{18} \ \frac{\int_{\Delta v} T_b(v)\, dv}{\mathrm{K\ \ km\ s^{-1}}} \qquad (\tau \ll 1) \tag{5}$$

where the velocity range of the integral, Δv, corresponds to the velocity interval used in Equation (2). We assume that the WNM contribution to N is optically thin, so Equation (5) gives the relationship between N_w and the brightness temperature for this phase in a two-phase approximation (Equation (4)). The corresponding integral of the absorption spectrum gives the following:

$$\frac{N}{T}\left(\frac{\mathrm{K}}{\mathrm{cm}^{-2}}\right) = 1.82 \cdot 10^{18} \ \frac{\int_{\Delta v} \tau(v)\, dv}{\mathrm{km\ s^{-1}}} \tag{6}$$

where T on the left side would be the excitation temperature of the line if all the gas were at the same temperature in the velocity range Δv. In the two-phase approximation of Equation (4), the left side of Equation (6) becomes $\frac{N_{\mathrm{CNM}}}{T_{\mathrm{CNM}}}$, with N_{CNM} the column density of cool phase gas, and T_{CNM} the cool phase temperature (e.g., Dickey et al. 2003). Again, the atomic hydrogen shows variation in temperature of at least two orders of magnitude, so T_s does not represent a physical temperature, but rather a harmonic mean as in Equation (4). As such it is still a critically important quantity for understanding the relative fractions of warm and cool phases. A common use (e.g., Murray et al. 2020) is to derive f_c, the fraction of cool phase H I by mass:

$$f_c \ \equiv \ \frac{N_{\mathrm{CNM}}}{N_{\mathrm{CNM}} + N_{WNM}}. \tag{7}$$

If the optical depth is small, then f_c is simply as follows:

$$f_c = \frac{T_{\mathrm{CNM}}}{T_s} \quad (\tau \ll 1) \tag{8}$$

where T_{CNM} is the cool phase excitation temperature, typically assumed to be 50–100 K based on results like those of Heiles & Troland (2003) and Murray et al. (2018). If the optical depth is not small, then warm gas can be hidden behind the CNM. The two extremes are that all the WNM is behind all the CNM, and all the WNM is in front of the CNM. They give lower and upper limits on f_c, respectively:

$$\frac{\tau}{\tau \ + e^{\tau} \cdot \left(\frac{T_b}{T_{\mathrm{CNM}}} - \frac{T_b}{T_s}\right)} \ \leqslant \ f_c \ \leqslant \ \frac{\tau}{\tau \ + \frac{T_b}{T_{\mathrm{CNM}}} - \frac{T_b}{T_s}} \tag{9}$$

given the observed T_b and T_s and an assumed value of T_{CNM}. For a typical case where half the WNM is in front of the CNM and half behind, then the simple formula of Equation (8) is accurate to a few percent for $\tau \sim 1$. For the analysis that follows, we ignore self-absorption and compute T_s from Equation (3) with the two-phase assumption of Equations (4)–(6), and leave more complex radiative transfer modeling to a future paper when the GASKAP emission spectra are available.

By comparing the emission as a function of latitude, averaged over the area of the ASKAP field and over the same velocity intervals as for the absorption, we can compute the mean spin temperature of the gas, T_s, and estimate the cool phase temperature, T_{CNM}.

The profile labeled "emission" on the right-hand panel of Figure 5 is an average of the emission spectra in the HI4PI survey (HI4PI Collaboration et al. 2016). The HI4PI data in this area come from the Parkes GASS survey (McClure-Griffiths et al. 2009), and they have been carefully corrected for stray radiation (Kalberla et al. 2010); thus the emission spectra are trustworthy down to a small fraction of a Kelvin in brightness temperature. For Figure 5, we average data from a

rectangle defined by the black lines in Figure 2; at each latitude, we average the emission over the longitudes within the PAF footprint. For comparison with the absorption, we scale the emission so that the peak coincides with the peak in the weighted Gaussian fit to the measured absorption points. The scale factor is $1/158$ K $= 45.8/0.29$, as the emission peak is 45.8 K while the maximum absorption $(1 - e^{-\tau}) = 0.29$. If the H I gas were all at the same temperature, i.e., a one-phase assumption, then $T = T_s = 158$ K and the emission and absorption profiles should look the same after this scaling.

At first glance, the emission does look roughly the same as the absorption in the right panel of Figure 5, but the width (in latitude) of the emission is broader than the Gaussian fitted to the absorption, and at latitudes above $|b| \simeq 1°$, the emission is well above the absorption fit. This would naturally result if the emission includes a contribution from the WNM with a broader scale height than the CNM seen in absorption, as

$$T_b = T_{b,WNM} + T_{\rm CNM}(1 - e^{-\tau}) \quad (10)$$

where $T_{b,WNM}$ is the emission due to the WNM, and the second term on the right is the contribution of the CNM to the emission brightness temperature, T_b. Fitting the emission profile with two Gaussians shows how much WNM versus CNM is needed. We force the emission from the CNM component to have the same center and width in latitude as the absorption, and fit a Gaussian to the WNM component using only the data with $|b| > 1°.2$. The result is shown on the last line of Table 1. The Gaussian fitted to the emission wings has width $\sigma_b = 1°.6$ and peak $T_b = 10.7$ K centered at $b = +0°.1$. The remaining emission is due to the CNM, with peak 45.8–10.7 = 35.1 K. At midplane the CNM constitutes $35.1/45.8 = 77\%$ of the total H I, but above $|b| = 1°.5$, the H I is nearly all in the WNM phase. We can estimate the mean spin temperature of the CNM by dividing its contribution to the emission at midplane, 35.1 K, by the peak value of $\langle 1 - e^{-\tau} \rangle$, i.e., $35/0.29 = 121$ K (bottom line of Table 1).

Even with this two-phase analysis, the 121 K result for the CNM mean spin temperature represents a blend of H I temperatures. The molecular phase is so dominant in the inner Galaxy that a significant fraction of the atomic hydrogen may be mixed in or between the molecular clumps, with spin temperature in equilibrium with the kinetic temperature of ~50 K or less, similar to T_s values found in the Perseus molecular cloud by Stanimirović et al. (2014). The 121 K value would then result from a blend of such very cold H I with some warmer gas, at spin temperatures of 50 K to several hundred Kelvins. Careful analysis of individual absorption features combined with the high-resolution GASKAP emission cubes may further clarify the temperature distribution of the CNM in the 3 kpc Arm and near the far end of the bar. Study of the GASKAP emission cube will be the topic of the next paper in this series.

Figure 6 shows plots of $1 - e^{-\tau}$ versus latitude as in Figure 5, but now for Δv intervals at positive velocities, corresponding to gas near the solar circle, and then progressively farther outside the solar circle on the far side of the Galactic center. The left panel shows absorption, $\langle 1 - e^{-\tau} \rangle_{\Delta v}$, versus latitude for velocity range $\Delta v = [0, +8]$ km s^{-1}. The CNM that causes absorption in this velocity range is partly in the solar neighborhood, and partly at or just beyond the solar circle at a distance of 15.6 $\frac{R_o}{8.31\rm kpc}$ kpc. The local gas is spread very widely in latitude, so widely that $\langle 1 - e^{-\tau} \rangle$ is roughly constant for $-3° < b < +3°$, while the distant CNM has a Gaussian shape with width $\sigma_b = 0°.59$, similar to the width at the tangent point. Since this gas is twice as far away, the physical scale height of the CNM cloud population must be about 160 pc, for a full width to half-maximum CNM cloud layer about 375 pc thick. The peak of the Gaussian corresponding to the far side feature, $1 - e^{\tau} = 0.37$, is quite similar to the baseline level, $1 - e^{-\tau_o} = 0.34$, due to the local CNM (blue curve in Figure 6), and similar to the results of surveys of absorption in the nearby molecular clouds (Nguyen et al. 2019).

The right panels of Figure 6 show profiles through the disk at much greater Galactic radii, $R \sim 12$ kpc for the upper panel and $20 < R < 40$ kpc for the lower panel. The upper panel shows that there is abundant CNM in the Sgr-Car arm at about 25 km s^{-1}. The baseline that was prominent due to local gas on the left panel, $(1 - e^{-\tau_o}) = 0.34$, has disappeared at these higher-positive velocities, and the CNM layer is continuing to flare, since the angular width, $\sigma_b \simeq 0°.56$, gives $\sigma_z = 200$ pc for a distance of 20 kpc ($R = 1.5R_o$).

The lower panel on the right side of Figure 6 shows that at $R > 3R_o$ the situation changes considerably. There is still a population of CNM clouds, but their aggregate optical depth is much smaller, and their scale height is much greater. Taking distance 33 kpc ($R \sim 4R_o$) and the scale height given by the Gaussian fit, $\sigma_b \simeq 1°.3$, gives σ_z about 750 pc. The CNM traces the flaring of the disk just as the H I emission does (Kalberla & Dedes 2008, their Figure 7). At this point, the optical depth on each LoS is so small that we need to stack (co-add) the spectra to get sufficient signal-to-noise to study the relationship between the emission and the absorption in this very distant gas.

4. The Outer Disk

Moving radially across the MW outer disk, far outside the solar circle, the H I is the dominant ISM constituent, and the 21 cm line is the only tracer of the structure and dynamics of the gas. Using the emission and absorption together, we can determine the conditions in the gas, at least as far as the mass fractions of CNM and WNM. A convenient quantity to use is the ratio of emission to absorption, i.e., T_s (Equation (3)). Although it does not measure the kinetic temperature nor even the excitation temperature of the gas, since it is always a weighted average of warm and cool phases (Equation (4)), T_s is a convenient indicator of the presence or absence of cool clouds in the warm, partially ionized surrounding gas (Bland-Hawthorn et al. 2017) that may include recently accreted circum-galactic material (Stewart et al. 2011; Trapp et al. 2022). For a rough estimate of the mass ratio of the phases, f_c (Equation (7)), we only need to know T_s and an estimate of $T_{\rm CNM}$, the cool phase temperature, predicted by, e.g., Bialy & Sternberg (2019, their Figure 6). Even without knowing $T_{\rm CNM}$ or f_c, we can use T_s to convert between the column density, Equation (5), and the equivalent width, Equation (6), for example, to interpret the results of extragalactic absorption line surveys (e.g., FLASH Allison 2021), since T_s is defined as the ratio of emission to absorption (Equation (3)).

In the outer Galaxy, far outside the solar circle, kinematic distances depend hardly at all on the choice of rotation curve. A simple, flat rotation curve, with $\Theta(R_o) = R\,\Omega(R_o) = \Theta_o$, gives very nearly the same distance versus radial velocity, v_r, as the Brand & Blitz (1993) or the Reid et al. (2014); in

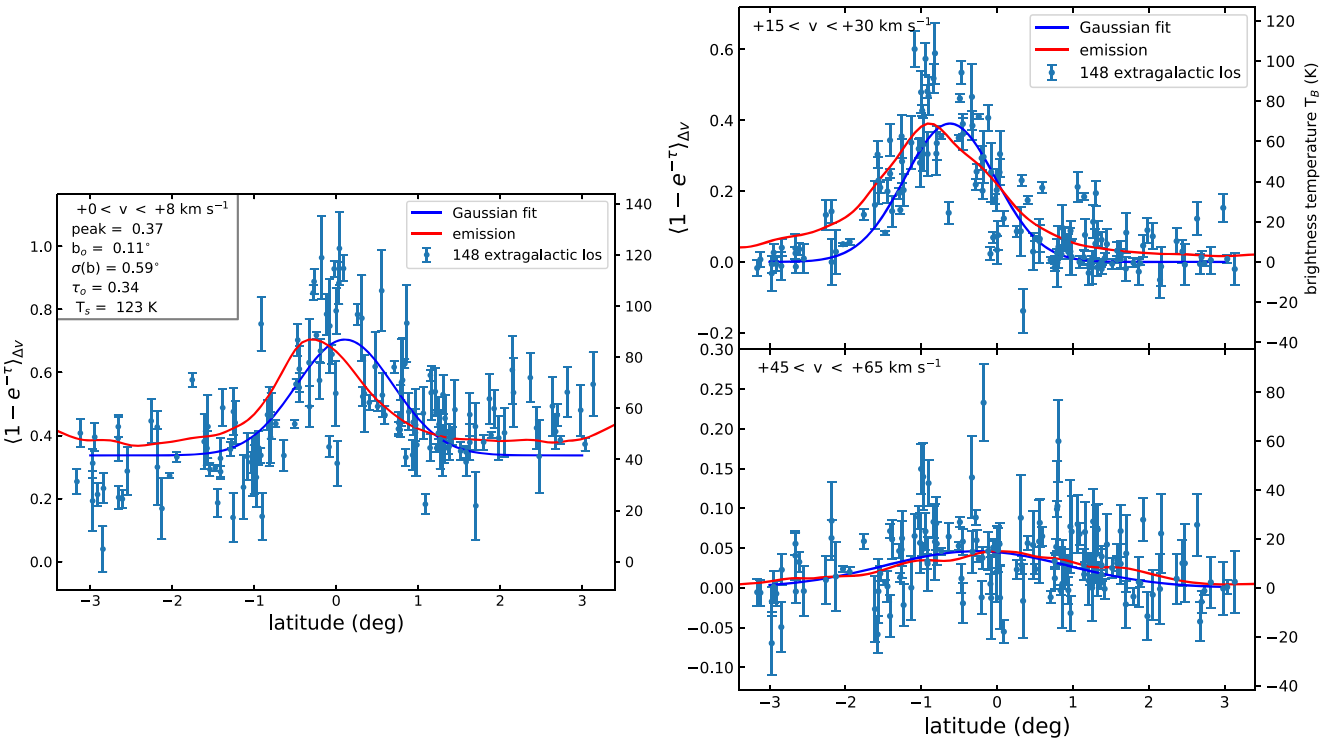

Figure 6. Mean absorption vs. latitude at the solar circle and beyond. The left panel shows the latitude dependence of the absorption at velocities near 0 km s^{-1}, which selects gas at the solar circle both in the solar neighborhood and on the far side of the Galaxy. The two right panels show the latitude dependence of the absorption beyond the solar circle on the far side of the Galaxy. The upper panel displays the velocity range $+15 < v < +30$ km s^{-1}, which includes the Sgr-Car Arm at velocity $\sim$+25 km s^{-1} and distance about 20 kpc. The lower panel shows the velocity range +45 to +65 km s^{-1}.

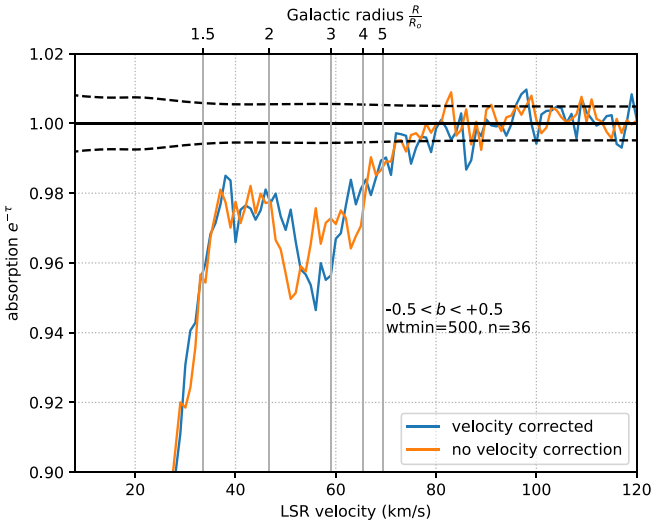

Figure 7. The effect of aligning spectral features at the same distance by shifting the velocity scales before averaging, using a factor of $\frac{\sin(\ell)}{\sin 340^\circ}$ (Equation (12)). The spectra are weighted averages of the 36 absorption spectra with the lowest noise ($\sigma_\tau < 0.045$) at low latitudes ($-0.5 < b < +0.5$). The velocity-corrected spectrum is the average after adjusting the velocity scales using Equation (12), the other is the average without adjusting. The faint absorption line at $v \sim +55$ km s^{-1} is narrower in the velocity-corrected stack, indicating that many of the 36 LoS contributing to the average at different longitudes all show absorption due to CNM at roughly the same distance. The upper scale on the x-axis shows the corresponding kinematic galactocentric radius, R.

Reid & Menten (2019), the A5 model curves, using the same solar neighborhood parameters, $\Theta(R) = \Theta_o = 240$ km s^{-1}, and $R_o = 8.31$ kpc. At longitude $\ell = 340°$, the difference in velocity predicted by the A5 curve and a flat curve is only 0.3 km s^{-1} at $R = 20$ kpc, increasing to just 0.45 km s^{-1} at $R = 40$ kpc. In this section, we use the flat curve to estimate distances for absorption features at positive velocities, i.e., beyond the solar circle on the far side of the Galaxy.

Using a flat rotation curve, kinematic distances vary as sin (ℓ) simply due to the change in the projection of the LSR velocity along the LoS:

$$v_r = \Theta_o \left[\frac{R_0}{R} - 1 \right] \sin(\ell) \cos(b) \tag{11}$$

becomes

$$\frac{v_r}{\Theta_o \sin(\ell)} = \left[\frac{R_0}{R} - 1 \right] \tag{12}$$

at latitude $b = 0$, where v_r is the observed LSR velocity of a spectral feature, and R is its galactocentric radius. We adjust the velocity scales of all the spectra by multiplying the velocities by $\frac{\sin \ell}{\sin(340^\circ)}$ to align features at the same distance but different longitudes to the same standard velocity scale, i.e., Equation (12) with $\ell \equiv 340°$. Figure 7 shows the effect of this correction for the average of the 36 highest sensitivity spectra toward extragalactic sources with latitude $-0^\circ.5 < b < +0^\circ.5$. The result is that the broad, noisy feature, between about 45 and 65 km s^{-1} in the raw average, narrows to a width of about 5 km s^{-1} centered at about 55 km s^{-1}, a kinematic Galactic radius $R \simeq 3R_0$ or $\sim$25 kpc. Kinematic distances become quite uncertain at large R because the velocity gradient is small; $\frac{dv}{dR} \sim 0.5$ km s^{-1} kpc^{-1} at $\ell = 340°$ and $R = 4R_o$, so that random motions of $\sim$5 km s^{-1} can give errors in R of 10 kpc. In spite of this uncertainty, it is worthwhile to shift all spectra to a common

distance scale using Equation (12) before stacking so that absorption features at the same distance will align in velocity.

The spectra shown in Figure 7 are weighted averages,

$$\langle S(v)\rangle = \frac{\sum_i w_i \times S_i(v)}{\sum_i w_i}, \quad (13)$$

where $S_i(v)$ are the absorption spectra ($e^{-\tau}(v)$), and the weights w_i are inversely proportional to the off-line rms noise, σ_i, squared:

$$w_i = \frac{1}{\sigma_i^2}. \quad (14)$$

The error envelope of this average spectrum is the weighted average of the noise spectra, given by

$$\langle E(v)\rangle = \frac{\sqrt{\sum (w_i \times E_i)^2}}{\sum_i w_i} \quad (15)$$

where the individual spectra $S_i(v)$ and their respective noise envelopes, $E_i(v)$, have been shifted by $\frac{\sin(\ell)}{\sin 340^\circ}$ as discussed above. For the averages analyzed in this section, the maximum allowed weight is 900, spectra with lower noise are weighted by 900, so that a small number do not dominate the average. Spectra with weight less than 10 ($\sigma_\tau > 0.31$) are not used in the averaging at all.

For comparison with 21 cm emission, we use the HI4PI compendium of surveys (HI4PI Collaboration et al. 2016), taking spectra at the same positions as the absorption spectra, and using the same weights (w_i) to compute the average emission. The 64 m Parkes telescope, which provided all the data in HI4PI at these declinations, does not have a high enough gain to detect the absorption toward the very compact emission of the extragalactic background sources. Some of the Galactic continuum sources are surrounded by extended continuum emission. For these a careful comparison of emission and absorption will require the full ASKAP emission maps. But to study the absorption in the outer Galaxy, we use only the extragalactic continuum source sample.

4.1. Absorption Lines

There are not enough background sources in the GASKAP field to allow the mapping of the spatial distribution of the CNM gas that causes the absorption in the outer Galaxy. For a rough, low-resolution study of the continuity of the absorbing clouds over the field, we divide the area into six subfields of roughly equal areas: two longitude ranges, $336^\circ < \ell < 340^\circ$ (low longitudes) and $340^\circ < \ell < 344^\circ$ (high longitudes), for each of three latitude ranges, $-3^\circ < b < -1^\circ$ (negative latitudes), $-1^\circ < b < +1^\circ$ (low latitudes), and $+1^\circ < b < +3^\circ$ (positive latitudes). The stacked spectra for each region are shown in Figures 8, 9, and 10.

Almost all the regions show a distinct absorption line centered at about +20 km s^{-1}, with the exception of the region at positive latitude ($+1^\circ < b < +3^\circ$) and lower longitudes ($335^\circ < \ell < 340^\circ$); see Figure 10, left panel. Two blended, narrow lines centered at about +60 and +65 km s^{-1} that are prominent in the right-hand panel of Figure 10 (positive latitudes and higher longitude) are seen faintly in the low latitudes at high longitudes and very faintly in the lower longitudes at positive latitudes but not elsewhere. The spectrum at low latitudes and high longitudes, Figure 9, right-hand panel, shows a feature centered on ∼+58 km s^{-1}, also clearly seen in Figure 7. At negative latitudes and low longitudes, there are two features between +45 and +55 km s^{-1}, as in Figure 8, left panel.

4.2. Warm and Cool Phases at Large R

Two examples of clouds detected on specific LoS at high positive velocities are shown in Figure 11. Gaussian fits to $e^{-\tau}$ are shown. For the narrower line, with $\sigma_v \simeq 1.7$ km s^{-1}, the implied upper limit kinetic temperature is $T_D = 340$ K, from

$$\frac{T_D}{\mathrm{K}} = 121 \left(\frac{\sigma_v}{\mathrm{km\ s^{-1}}}\right)^2 \quad (16)$$

where σ_v is the fitted velocity dispersion of the absorption line. Generally the line width has a turbulent contribution as well as the Maxwellian thermal velocity width, so that T_s is typically less than half of T_D (e.g., Jameson et al. 2019; Murray et al. 2018). The red curves of Figure 11 represent the HI4PI emission, plotted upside down and scaled by 50 K^{-1}. In both cases, the absorption goes well below the emission, which indicates that the spin temperatures of the clouds are less than 50 K. Since the HI4PI emission is based on the GASS Parkes survey with a beamwidth of 14′, the emission-absorption comparison on a single LoS is tentative; a more accurate spin temperature analysis will be possible with the full-resolution emission cube from ASKAP.

These CNM clouds are similar to the large, cool clouds found at high R in the second quadrant by Strasser et al. (2007). Most of the Strasser et al. clouds show mean spin temperatures between 60 and 120 K (their Table 3) and Galactic radii R in the range 12 to 27 kpc. The clouds in Figure 11 are more distant ($R \simeq 27$ to 42 kpc) but otherwise consistent with the properties of the clouds in that survey.

To estimate the radial variation of the mean spin temperature, i.e., the ratio of emission divided by absorption in Equation (3), we consider the two averages of absorption and emission spectra, shown in the two panels of Figure 12. The left panel is the weighted average of all 175 spectra toward extragalactic sources with noise $\sigma_\tau < 0.32$, giving weight $w_i > 10$ in Equation (14). The emission spectra and the optical depth noise spectra are averaged using the same weights, as for Figures 8, 9, and 10. This grand average has an optical depth noise $\sigma_\tau = 0.0042$ in each 1 km s^{-1} velocity channel. Averaging channels in groups of five reduces the noise to 0.0030. Since the emission (red curve) is about 0.05 * 200 = 10 K in the velocity range 40–70 km s^{-1}, and the absorption is $\tau \sim (1 - e^{-\tau}) \sim 0.035$, mean spin temperatures are in the range 260 to 310 K (one sigma). The radiometer noise in the weighted average emission spectrum is insignificant: the discrepancy in beam size between the emission and absorption is the main source of uncertainty, as discussed above. The mean spin temperatures computed for the 5 km s^{-1} averages are shown as the green crosses on the left panel of Figure 12. For velocities between 20 and 30 km s^{-1} corresponding to the Sagittarius-Carina (Sgr-Car) Arm, the mean spin temperatures are relatively low, $T_s = 170$ and 160 K, similar to solar neighborhood values seen at high latitudes (Heiles & Troland 2003; Murray et al. 2018). Beyond about 35 km s^{-1}, nominal $R \simeq 15$ kpc, the mean spin temperatures rise to the range 250–400 K, out to velocity 65 km s^{-1}, nominal $R = 40$ kpc. Beyond 70 km s^{-1}, the mean spin temperature rises to about 450–500 K, but the absorption is barely

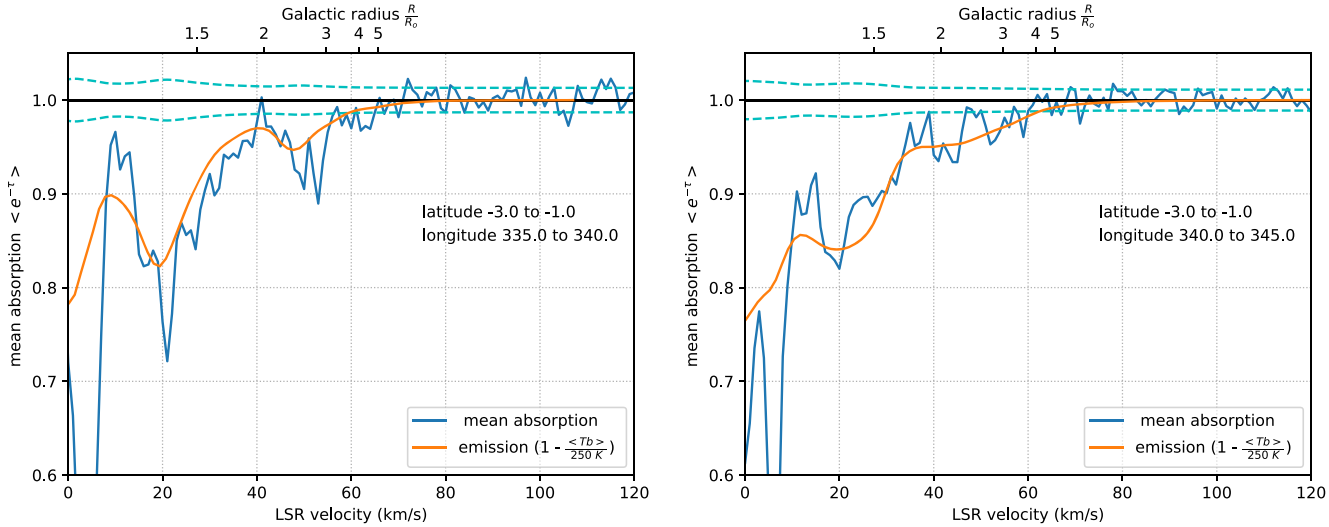

Figure 8. Averages of spectra at negative latitudes $-3° < b < -1°$, with the lower longitudes on the left ($335° < \ell < 340°$) and the higher longitudes on the right ($340° < \ell < 345°$). The weighted average absorption spectrum is shown, and the similarly weighted average emission, $\langle T_b \rangle$, is shown, scaled to match the nominal absorption at $T_s = 250$ K. If $T_s < 250$ K, then the absorption profile is below the scaled emission; if $T_s > 250$ K, then the absorption is above the emission. The noise envelopes shows $\pm 1\sigma$ assuming the spectra are independent. The upper scale on the x-axis shows the kinematic galactocentric radius, R, in units of the solar circle radius, R_0, assuming a flat rotation curve.

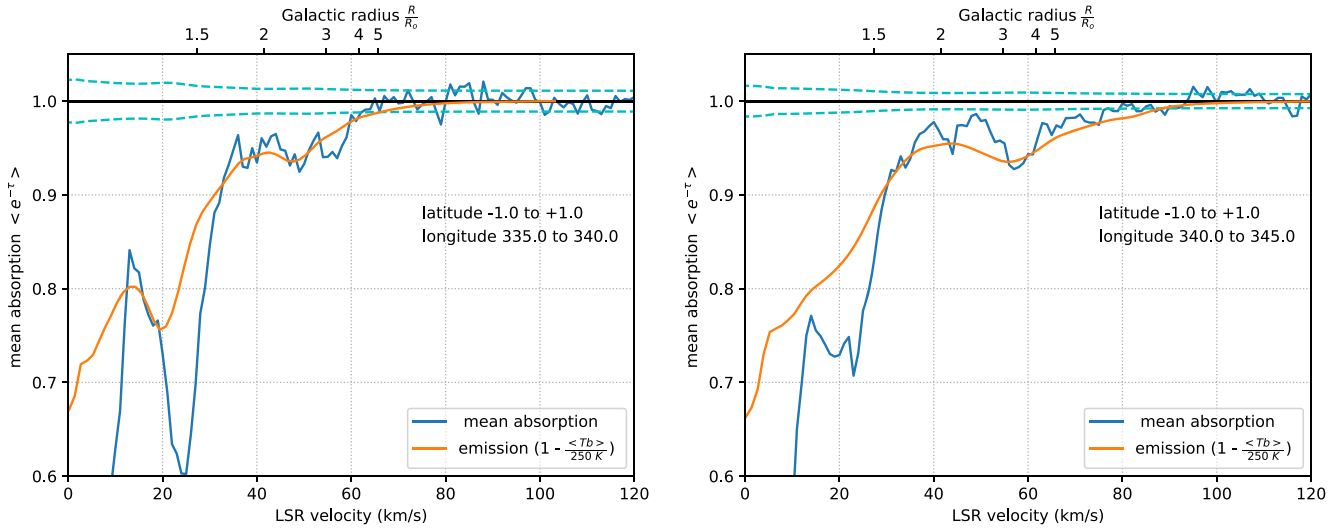

Figure 9. Averages of spectra at low latitudes, $-1° < b < +1°$, with the lower longitudes on the left ($335° < \ell < 340°$) and the higher longitudes on the right ($340° < \ell < 345°$), as in Figure 8. In this case, the absorption in the Sgr-Car Arm with v between 20 and 30 km s^{-1} is mostly much cooler than the nominal $T_s = 250$ K used for scaling the emission, but 250 K is typical for the very distant gas at $50 < v < 65$.

detected at these velocities, and the translation between velocity and R is compromised by the random motions of a few km s^{-1}.

Table 3 gives values derived from the average spectra in the left panel of Figure 12. Each row on the table corresponds to a velocity interval of 5 km s^{-1}, indicated in the first column. The galactocentric radius, R, of the midpoint of the interval is given in the second column, and the length along the LoS, Δd, corresponding to this velocity interval is given in the third column. The mean value of the absorption over the interval with error is in column four, i.e., the equivalent width. The mean brightness temperature of the emission average is in column five. The mean spin temperature computed with these two means is in column six, with errors based on the errors in the optical depth. Using the path length, Δd and the absorption and emission averages times the velocity interval width, we get the column density divided by path length, i.e., the mean density of H I from the emission spectrum, column eight in Table 3, and from the equivalent width, we get a mean value for the density divided by the mean spin temperature in column seven (Dickey et al. 2009, their Equations (5) and (6)). Both these quantities change by nearly two orders of magnitude from $R \sim 10$ to $R \sim 40$ kpc, but their ratio, i.e., T_s, stays remarkably constant. The determination of R for last two rows on the table, $\Delta v = [65, 70]$ and $[70, 75]$ km s^{-1}, is not at all trustworthy, so values derived using distance are not given.

The right panel of Figure 12 shows the result for a small sample of spectra with very low noise ($w_i > 800$ or $\sigma_\tau < 0.035$), which are also selected by having significant absorption lines in the range 48–65 km s^{-1}. Thus this is a small and biased sample, selected to show the characteristics of the absorption at $R \simeq 25$ to 30 kpc. At those velocities, the absorption line is prominent, and it leads to a particularly low value for T_s at $v = 55$–60 km s^{-1} that gives $T_s = 177 \pm 14$ K. In this case, the error bars are given not by the noise in the absorption spectrum but by the scatter in the

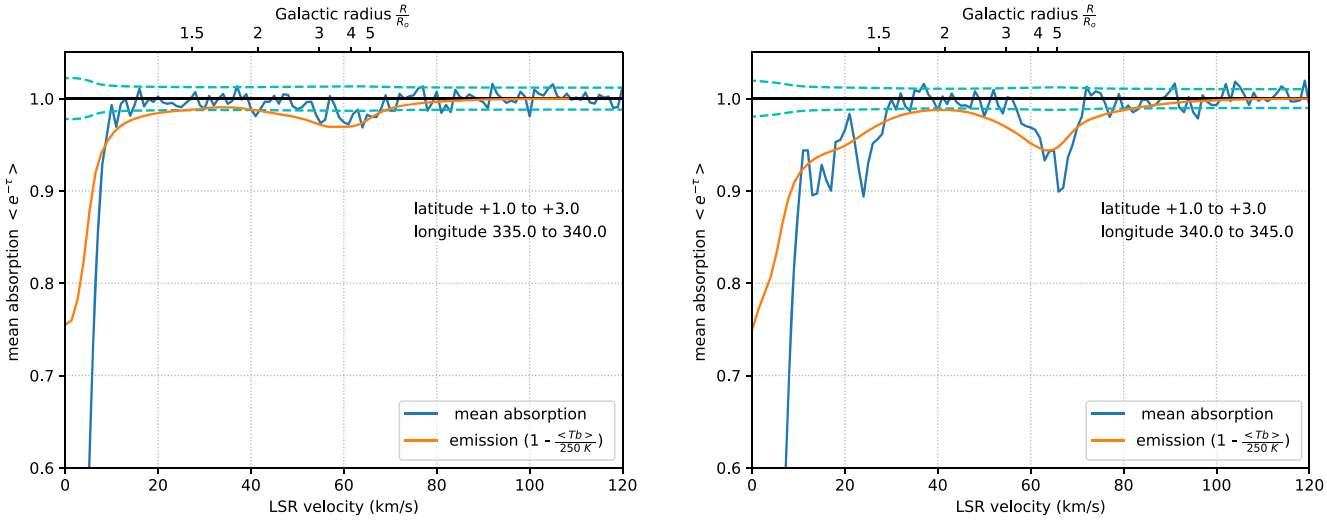

Figure 10. Averages of spectra at positive latitudes, $+1^\circ < b < +3^\circ$, with the lower longitudes on the left ($335^\circ < \ell < 340^\circ$) and the higher longitudes on the right ($340^\circ < \ell < 345^\circ$), as in Figure 8.

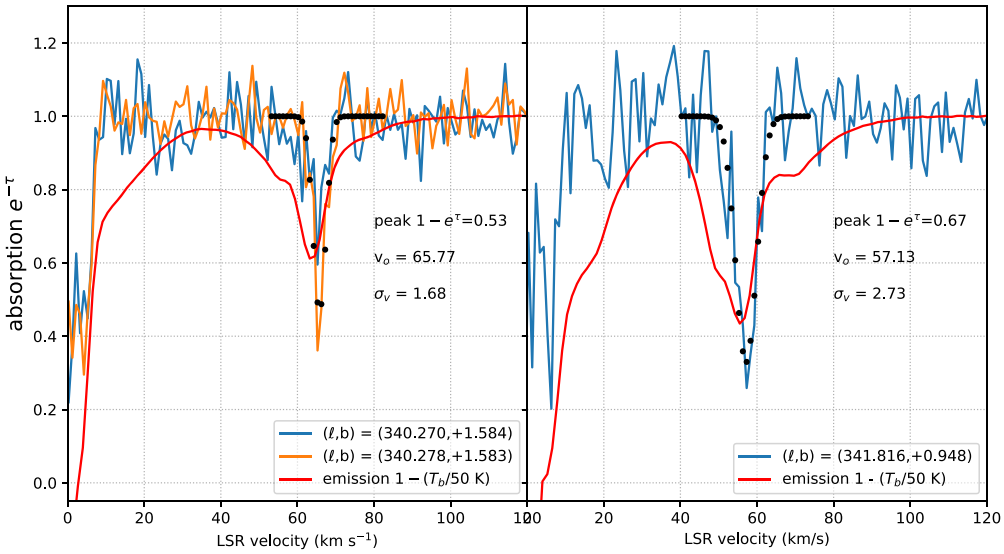

Figure 11. Representative absorption lines in the far outer Galaxy. The left panel shows absorption spectra toward two components of a double source at (ℓ, b) = (340.27, +1.58), the right panel shows the spectrum toward a source at (341.82,+0.95). Gaussian fits to the deeper line in the left panel and the line in the right panel are shown. The HI4PI emission spectra are plotted for comparison as $1 - \left(\frac{T_b}{50K}\right)$. Both absorption lines go below the emission at their lowest points, suggesting that the spin temperature is less than 50 K.

Table 3
Outer Galaxy Mean H I Spin Temperatures

Δv km s^{-1}	R kpc	Δd kpc	$\langle 1 - e^{-\tau} \rangle$	$\langle T_b \rangle$ K	T_s K	$\langle \frac{n}{T} \rangle$ 10^{-6} cm^{-3} / K	$\langle n \rangle$ 10^{-3} cm^{-3}
[15, 20]	10.5	0.8	0.169 ± 0.004	36.3	215^{+5}_{-5}	585.68 ± 14.14	126.13
[20, 25]	11.4	1.0	0.191 ± 0.004	31.8	167^{+4}_{-3}	567.90 ± 11.91	94.64
[25, 30]	12.5	1.2	0.137 ± 0.004	21.3	155^{+4}_{-4}	343.25 ± 9.11	53.34
[30, 35]	13.7	1.4	0.059 ± 0.003	13.4	229^{+14}_{-12}	121.90 ± 6.85	27.89
[35, 40]	15.3	1.7	0.030 ± 0.003	9.9	328^{+37}_{-30}	51.06 ± 5.21	16.77
[40, 45]	17.2	2.2	0.031 ± 0.003	9.3	298^{+32}_{-26}	41.46 ± 4.02	12.37
[45.50]	20	2.9	0.026 ± 0.003	10.4	396^{+52}_{-41}	26.80 ± 3.12	10.62
[50, 55]	23	3.9	0.033 ± 0.003	10.6	320^{+33}_{-27}	24.77 ± 2.30	7.92
[55, 60]	28	5.7	0.038 ± 0.003	10.2	264^{+23}_{-20}	19.85 ± 1.59	5.25
[60, 65]	35	9.0	0.029 ± 0.003	8.6	291^{+34}_{-27}	9.61 ± 0.99	2.80
[65, 70]	∼47	...	0.024 ± 0.003	6.0	253^{+36}_{-28}	...	...
[70, 75]	...	...	0.008 ± 0.003	3.8	485^{+274}_{-129}	...	...

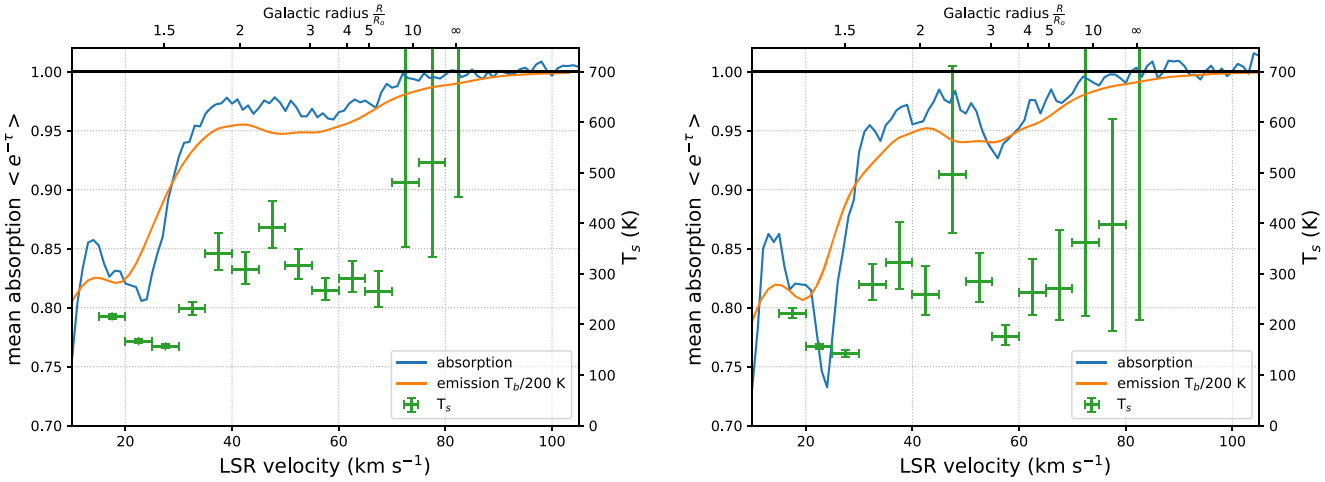

Figure 12. The variation with velocity of the mean spin temperature, computed as the ratio of the sample mean values of T_b and $1 - e^{-\tau}$. The corresponding values of Galactic radius, R, are indicated on the upper x-axis scale in units of R_o, the solar circle radius. The left panel shows overall averages of all 175 extragalactic background sources in the PAF field. The right panel shows the average for a subset of spectra with very low noise that show significant absorption lines in the range $55 < v < 66$ km s^{-1}.

values of $(1 - e^{-\tau})$ as the standard deviation of the sample of different spectra. The optical depth profile is the mean of the sample, i.e., the spectra are all given equal weight. In spite of the small sample and selection bias, this sample of LoS gives mean spin temperatures quite similar to the weighted average of the much larger sample on the left panel. On the right panel, T_s is in the range 250 to 400 K for $30 < v < 70$ km s^{-1}, except for the high value (500^{+220}_{-120} K) for v between 45 and 50 km s^{-1} and the artificially low value between 55 and 60 km s^{-1} due to the sample selection criteria.

On the right panel of Figure 12, it is interesting to consider the shape of the tail of the mean absorption spectrum at velocities between about 65 and 82 km s^{-1}, i.e., $40 < R < \infty$ in Equation (12). Possibly all the gas seen beyond 65 km s^{-1} is closer than $R \simeq 40$ kpc, and random motions, both microscopic and macroscopic, spread out the velocity distribution by 10 to 15 km s^{-1} in absorption and 25 km s^{-1} in emission. These two spectral tails appear to be exponential in their asymptotic behavior approaching one in the figure. For comparison, Kalberla & Kerp (2009) find, using the LAB survey data, that for $R > 35$ kpc the disk surface density of the H I, Σ, changes slope on a plot of log Σ - log R, and azimuthal symmetry breaks down (e.g., Kalberla & Dedes 2008, their Figure 9). At longitude 340°, $R = 35$ kpc corresponds to $v \simeq 63$ km s^{-1}. Thus the last velocity interval corresponding to distinctively disk gas from Figure 12 is 60 to 65 km s^{-1}.

A value of T_s about 300 K is consistent with the finding of Dickey et al. (2009, their Figure 5), but the result here is more precise because it is based on a much larger sample of spectra in a much smaller area. Typical values of T_s measured in extragalactic damped Lyman α systems are higher than the values measured here (Kanekar et al. 2014), but two systems with relatively high metallicity (Kanekar 2014) show mean spin temperatures of 372 K and (tentatively) 242 K. Thus conditions in the outer edge of the MW disk may be similar to low-redshift extragalactic 21 cm absorption systems (Allison 2021, and references therein).

5. Discussion

Physical interpretation of mean spin temperature measurements in the far outer disk of the MW is ambiguous; conditions in that environment are very different from those in the local ISM. Even in the solar neighborhood, the spin temperature may depart from the kinetic temperature of the gas, particularly in the WNM (Liszt 2001, 2002; Davies & Cummings 1975). The spin temperature will be driven to equal the kinetic temperature in low density environments by the Wouthuysen-Field effect, i.e., differential radiative excitation and de-excitation of the Ly α transition when the color temperature of the radiation has come into equilibrium with the kinetic temperature (Seon & Kim 2020, and references therein). Even if the excitation of the 21 cm line is in equilibrium with the neutral hydrogen kinetic temperature in all phases, values of T_s measured from comparison of the 21 cm emission and absorption represent a harmonic mean of different thermal phases (Equation (4)) at least including the CNM and WNM, often with UNM clouds as well (Murray et al. 2018) that may be more common in the outer disk than they are here. At the outer edge of the MW disk, even the existence of two equilibrium phases is in doubt, depending on the metallicity and the trade-off between heating by UV photons versus cosmic rays (Bialy & Sternberg 2019). The abundance of grains is also critical (Wolfire et al. 2003, Figure 13), since photoelectric heating dominates as long as the metallicity $Z' > 0.1$ (Bialy & Sternberg 2019, their Section 4). If the gas-phase abundance gradient derived from H II region temperatures by Wenger et al. (2019) continues as far as $R \simeq 35$ kpc, the oxygen abundance (O/H) would be $< \frac{1}{10}$ of its value at the solar circle. It may be that the gas we see in H I emission and absorption never has time to come to thermal equilibrium because of episodic shock heating due to converging flows (Vázquez-Semadeni et al. 2006; Gazol & Villagran 2016). Such events must be common in CGM gas, occurring at intervals not much longer than the cooling time. Giving up on thermal equilibrium, modern simulations provide models of the evolution of gas passing through a hot halo while condensing from WIM to WNM to CNM (Banda-Barragán et al. 2020; Nelson et al. 2020; Dutta et al. 2022). Such simulations indicate that cold-mode accretion can include both WNM and CNM clouds.

The connection between cool H I clouds at large R, like those seen in this study and the accretion of gas onto spiral disks, is considered by Bland-Hawthorn et al. (2017), with particular attention to the effects of the external ionizing radiation field. Both the CNM and WNM fit in the category of *cold-mode* accretion in this context, in contrast to *warm hot* and *hot mode* that are warmer

still, and fully ionized (Putman et al. 2012). In the models of Stewart et al. (2011) and Trapp et al. (2022), a likely accretion pattern is for corotating CGM gas to migrate inward through the outer boundary of the disk and on to the inner disk where star formation is active. Simulations, like that of Nuza et al. (2019), put this process along with accretion by vertical infall in context over cosmological timescales. The CGM seen in faint 21 cm emission with the Green Bank Telescope around many nearby spirals (Pisano 2014; Pingel et al. 2018; Martin et al. 2019; Das et al. 2020; Sardone et al. 2021) is the reservoir from which the cold-mode accretion flows. The structure, dynamics, thermodynamics, and ionization of the CGM are not yet fully understood; they present many compelling astrophysical questions that may ultimately tie together the physics of the ISM in spiral disks with the process of galaxy formation studied through cosmological simulations and high-redshift absorption line surveys.

5.1. Future Observations

The ASKAP Pilot survey observations were done in 2019/2020, to be followed by the second pilot phase in 2021, and full survey observations beginning in early 2022. Based on the absorption line results presented here, and the emission line cubes still being analyzed, the astrophysical drivers and survey strategy will be finalised. For the full survey, the GASKAP proposal (Dickey et al. 2013) plans 50 hr of integration time for each field in a single line of PAF footprints along the Galactic plane. This integration time will reduce the rms noise in every spectrum by a factor of 1.8 compared with the 16 hr Pilot Survey integration. Thus most of the spectra that currently have low weights ($100 < w_i < 300$, i.e., $0.06 < \sigma_\tau < 0.1$) would move to higher weights ($\sigma_\tau < 0.05$), and a larger number of new spectra would become available at low weights. This will more than double the number of spectra per square degree in each sample (Figures 8–10). The current sample is too sparse to map the distribution of the absorption. With a reduction in the noise level in all spectra by a factor of almost 2, it will be possible to grid the optical depths at each velocity into images of the structures that cause the absorption. This will be very helpful to determine the CGM cloud mass spectrum, turbulence spectrum, and CNM filling factor.

Observing farther above and below the Galactic plane is also part of the GASKAP survey strategy. To cover a larger latitude range, $3° < |b| < 10°$, in a reasonable time, the integration time per pointing would be ∼10 hr, shorter than for this Pilot field. Since the density of extragalactic sources is the same at all latitudes, those fields will give numbers of spectra and optical depth sensitivities very similar to those obtained here, but with σ_τ higher by 26%. At a distance of 35 kpc, the ±10 degree range in latitude becomes a range in height above and below the plane, z, of $-6 < z < +6$ kpc, enough to map the flaring of the CNM disk, i.e., the increase of the scale height with R. Comparison with the emission survey over this increased range of latitude would show whether heating and partial ionization by the external UV field (Bland-Hawthorn et al. 2017) causes a temperature gradient with z in the gas in the far outer disk. The results will help to explain how the CGM properties evolve as the cold-mode accretion flow brings corotating clouds into the thick disk and ultimately into the thin disk.

6. Summary

Study of H I absorption in a single pilot field observed with the ASKAP telescope at velocity resolution of 1 km s^{-1} gives a variety of results that demonstrate the power of the telescope and the potential of a full survey of the Galactic plane as part of the GASKAP project. This paper concentrates on analysis of the spectra toward ∼175 extragalactic sources to determine the distribution of CNM in the Galactic disk. There is much more data to analyze, particularly using the Galactic continuum sources and their spectra.

The main topic considered here is the structure of the MW disk near longitude $\ell = 340°$ as traced by the 21 cm absorption. The thickness of the disk measured near the subcentral point implies that the CNM at the far end of the bar and in the 3 kpc arm is very tightly confined in z (near midplane), with scale heights ∼50 pc. This is the first measurement of such a narrow scale height for the atomic medium in the inner Galaxy, in good agreement with molecular lines and the ultra-thin stellar disk (Section 3). Near the solar circle on the far side of the Galactic center, the scale height is ∼160 pc, similar to its value in the solar neighborhood.

Moving to the outer Galaxy, the disk continues to flare. The absorption spectra trace the CNM far outside the solar circle, to radius $R \sim 40$ kpc. Although kinematic distances become less accurate at large R, the CNM follows the WNM to the edge of the disk. The ratio of the emission and absorption is nearly constant versus velocity to at least $5R_o$.

The number of background sources giving sensitive absorption spectra is large enough that some structure in the outer disk is evident. Dividing the field into six regions shows that some have much more CNM than others at $25 < R < 40$ kpc. Some lines of sight show quite deep, narrow absorption lines at velocities of 55–70 km s^{-1}; two examples are presented. Comparison with emission in these directions suggests that the CNM temperature is less than 50 K in these clouds.

The GASKAP survey will extend our knowledge of the CNM beyond the disk and into the CGM where cold-mode accretion is underway. It will provide statistics of absorption lines for comparison with results from extragalactic surveys to help quantify the thermal balance in gas in exogalactic environments.

The Australian SKA Pathfinder is part of the Australia Telescope National Facility, which is managed by CSIRO. Operation of ASKAP is funded by the Australian Government with support from the National Collaborative Research Infrastructure Strategy. ASKAP uses the resources of the Pawsey Supercomputing Centre. Establishment of ASKAP, the Murchison Radioastronomy Observatory, and the Pawsey Supercomputing Centre are initiatives of the Australian Government, with support from the Government of Western Australia and the Science and Industry Endowment Fund. We acknowledge the Wajarri Yamatji people as the traditional owners of the Observatory site. This paper includes archived data obtained through the CSIRO ASKAP Science Data Archive, CASDA.

This research has made use of of NASA's Astrophysics Data System; the SIMBAD database and VizieR catalog access tool, CDS, Strasbourg, France (DOI: 10.26093/cds/vizier); and matplotlib for python (Hunter 2007).

Appendix
Continuum Source Positions

Positions of the continuum Galactic and extragalactic sources are given on Tables 4 and 5. The columns give the index number, ecliptic coordinates (J2000), Galactic coordinates, the rms noise in the absorption spectrum, and information about the structure and, for the Galactic sources on Table 4, the type of source.

Table 4
Galactic Sources

Index	R.A.	Decl.	Longitude	Latitude	σ_τ	Identification	Structure
3	16:30:25.8	−46:02:51	337.474	+1.619	0.472	Planetary Nebula	point
17	16:32:56.4	−47:57:54	336.367	−0.004	0.088	WISE-H II ATLASgal	point
20	16:32:57.5	−46:40:28	337.315	+0.872	0.126	SNR	mean of a double source
23	16:33:28.9	−47:29:53	336.772	+0.247	0.197	WISE-H II ATLASgal	complex structure
26	16:33:58.3	−46:50:09	337.314	+0.635	0.198	Planetary Nebula	point
29	16:34:04.7	−47:16:30	337.004	+0.324	0.034	WISE-H II ATLASgal	point
30	16:34:28.3	−47:52:52	336.603	−0.136	0.552	YSO?	point
31	16:34:33.9	−47:58:15	336.548	−0.208	0.426	ATLASgal	complex structure
32	16:34:38.4	−47:36:31	336.823	+0.028	0.274	ATLASgal	complex structure
33	16:34:39.5	−47:36:06	336.830	+0.030	0.133	ATLASgal	complex structure
34	16:34:48.4	−47:32:49	336.887	+0.049	0.077	WISE-H II ATLASgal	complex structure
35	16:34:53.0	−47:37:04	336.844	−0.008	0.194	YSO?	complex structure
36	16:35:12.8	−47:35:32	336.900	−0.032	0.092	WISE-H II ATLASgal	point
37	16:35:32.3	−47:31:14	336.990	−0.024	0.060	WISE-H II ATLASgal	point
43	16:36:13.5	−47:31:06	337.070	−0.108	0.271	dark cloud	point
44	16:36:24.8	−47:24:33	337.172	−0.058	0.088	WISE-H II ATLASgal	complex structure
46	16:36:28.4	−47:23:55	337.187	−0.059	0.091	WISE-H II	complex structure
48	16:36:30.9	−47:23:36	337.195	−0.061	0.804	WISE-H II ATLASgal	complex structure
50	16:36:42.5	−47:31:31	337.120	−0.174	0.008	WISE-H II ATLASgal	complex structure
51	16:36:44.1	−47:31:59	337.117	−0.182	0.009	WISE-H II ATLASgal	complex structure
52	16:36:47.1	−47:31:37	337.127	−0.184	0.018	WISE-H II	complex structure
56	16:37:05.6	−47:21:40	337.285	−0.111	0.039	WISE-H II ATLASgal	ring or shell source
58	16:37:13.5	−47:25:17	337.255	−0.168	0.040	WISE-H II ATLASgal	ring or shell source
59	16:37:17.2	−47:23:47	337.281	−0.159	0.080	WISE-H II ATLASgal	complex structure
60	16:37:21.8	−46:11:30	338.184	+0.639	0.175	YSO	point
63	16:37:52.0	−46:54:34	337.708	+0.094	0.028	WISE-H II ATLASgal	one component of double
64	16:37:54.7	−46:54:46	337.711	+0.086	0.042	WISE-H II ATLASgal	one component of double
66	16:38:11.1	−47:04:52	337.617	−0.062	0.021	WISE-H II ATLASgal	complex structure
69	16:38:18.9	−47:04:51	337.632	−0.078	0.236	ATLASgal	point
72	16:38:30.9	−47:00:50	337.705	−0.059	0.026	WISE-H II ATLASgal	complex structure
75	16:38:50.4	−47:28:03	337.404	−0.402	0.371	WISE-H II ATLASgal	complex structure
76	16:38:52.3	−47:07:17	337.665	−0.176	0.017	WISE-H II ATLASgal	point
79	16:39:03.4	−46:42:27	337.995	+0.077	0.056	WISE-H II ATLASgal	point
82	16:39:21.6	−46:44:18	338.006	+0.018	0.095	WISE-H II ATLASgal	point
83	16:39:32.5	−46:55:26	337.889	−0.129	0.285	YSO	complex structure
85	16:39:38.8	−46:41:26	338.075	+0.013	0.009	WISE-H II ATLASgal	mean of a double source
86	16:39:49.6	−46:43:01	338.075	−0.028	0.105	WISE-H II ATLASgal	point
87	16:39:57.5	−46:45:10	338.064	−0.069	0.027	WISE-H II ATLASgal	point
89	16:39:59.7	−46:24:33	338.325	+0.155	0.062	ATLASgal	point
92	16:40:07.3	−46:23:26	338.353	+0.151	0.029	ATLASgal	complex structure
93	16:40:07.5	−46:25:06	338.333	+0.132	0.028	ATLASgal	point
96	16:40:10.4	−46:24:19	338.348	+0.135	0.196	ATLASgal	complex structure
97	16:40:11.0	−46:21:39	338.383	+0.163	0.029	YSO	complex structure
98	16:40:15.4	−45:39:03	338.922	+0.625	0.030	YSO	point
100	16:40:46.2	−46:24:36	338.413	+0.054	0.087	ATLASgal	complex structure
101	16:40:47.4	−46:32:00	338.323	−0.030	0.170	SNR	point
102	16:40:50.3	−46:23:24	338.436	+0.059	0.007	ATLASgal	point
103	16:40:55.2	−45:50:56	338.850	+0.406	0.102	WISE-H II ATLASgal	point
105	16:40:57.5	−46:21:34	338.472	+0.064	0.132	SNR	complex structure
106	16:40:58.1	−46:25:52	338.420	+0.015	0.207	YSO	complex structure
107	16:40:58.4	−46:27:00	338.406	+0.002	0.037	YSO	complex structure
108	16:40:59.3	−47:07:13	337.905	−0.444	0.071	S36 bubble	complex structure
109	16:41:01.6	−46:25:18	338.433	+0.014	0.007	ATLASgal	complex structure
110	16:41:03.9	−46:22:11	338.477	+0.043	0.068	SNR	mean of a double source
111	16:41:06.3	−46:21:32	338.489	+0.045	0.093	ATLASgal SNR	complex structure
114	16:41:06.4	−47:07:52	337.910	−0.466	0.005	WISE-H II	complex structure
113	16:41:08.2	−47:06:46	337.928	−0.458	0.015	WISE-H II ATLASgal	complex structure
116	16:41:13.2	−46:11:31	338.628	+0.140	0.026	WISE-H II ATLASgal	ring or shell source
121	16:41:16.1	−45:48:53	338.916	+0.383	0.054	WISE-H II ATLASgal	point
122	16:41:31.1	−46:34:31	338.374	−0.151	0.025	WISE-H II ATLASgal	point
124	16:41:36.2	−46:17:54	338.592	+0.021	0.035	ATLASgal	complex structure
125	16:41:43.5	−46:18:44	338.595	−0.005	0.126	WISE-H II ATLASgal	complex structure
126	16:41:44.3	−46:44:45	338.271	−0.293	0.156	WISE-H II ATLASgal	point

Table 4
(Continued)

Index	R.A.	Decl.	Longitude	Latitude	σ_τ	Identification	Structure
128	16:41:51.7	−46:35:08	338.405	−0.202	0.005	WISE-H II ATLASgal	ring or shell source
131	16:41:54.2	−46:34:58	338.412	−0.206	0.018	WISE-H II ATLASgal	point
132	16:42:01.2	−46:47:52	338.264	−0.363	0.128	WISE-H II	point
134	16:42:09.3	−46:47:03	338.289	−0.371	0.056	WISE-H II ATLASgal	point
136	16:42:14.1	−46:25:25	338.569	−0.144	0.024	WISE-H II ATLASgal	one component of double
137	16:42:19.2	−46:34:47	338.461	−0.258	0.093	WISE-H II ATLASgal	complex structure
138	16:42:23.9	−46:21:04	338.642	−0.118	0.153	IR emission lines?	point
139	16:42:24.0	−46:18:01	338.681	−0.084	0.059	ATLASgal	point
144	16:42:48.6	−45:54:06	339.028	+0.124	0.227	YSO	point
145	16:42:59.5	−45:49:40	339.104	+0.149	0.038	WISE-H II ATLASgal	complex structure
150	16:43:15.7	−44:35:17	340.071	+0.927	0.047	WISE-H II ATLASgal	point
158	16:44:14.0	−45:31:23	339.476	+0.185	0.071	WISE-H II ATLASgal	complex structure
166	16:44:41.0	−45:34:32	339.488	+0.091	0.060	WISE-H II ATLASgal	complex structure
168	16:44:49.2	−45:59:10	339.193	−0.195	0.017	pulsar	point
169	16:45:03.0	−45:30:34	339.580	+0.086	0.048	WISE-H II	complex structure
170	16:45:05.8	−45:30:13	339.590	+0.083	0.077	WISE-H II ATLASgal	complex structure
176	16:45:37.7	−45:22:37	339.747	+0.095	0.192	WISE-H II ATLASgal	point
178	16:45:51.1	−45:09:52	339.934	+0.204	0.235	YSO	point
180	16:46:08.8	−46:29:01	338.965	−0.693	0.119	SF cloud	mean of a double source
190	16:47:05.5	−45:50:36	339.558	−0.402	0.026	WISE-H II	complex structure
193	16:47:36.3	−45:45:47	339.678	−0.419	0.268	YSO	point
196	16:48:05.1	−45:05:11	340.249	−0.046	0.058	WISE-H II ATLASgal	point
198	16:48:10.6	−45:21:32	340.050	−0.234	0.016	WISE-H II ATLASgal	ring or shell source
202	16:48:14.3	−45:21:40	340.056	−0.244	0.027	WISE-H II ATLASgal	complex structure
208	16:48:53.5	−45:10:08	340.277	−0.208	0.035	ATLASgal	complex structure
212	16:49:14.8	−45:36:32	339.980	−0.539	0.131	ATLASgal	point
215	16:49:29.9	−45:17:46	340.248	−0.372	0.091	WISE-H II ATLASgal	complex structure
220	16:51:14.4	−46:14:21	339.717	−1.208	0.047	WISE-H II	complex structure
227	16:52:21.2	−44:27:58	341.210	−0.231	0.018	WISE-H II	ring or shell source
229	16:52:33.1	−43:23:46	342.059	+0.420	0.006	WISE-H II ATLASgal	complex structure
234	16:52:52.3	−43:54:22	341.702	+0.052	0.021	WISE-H II ATLASgal	point
235	16:52:54.7	−44:26:53	341.287	−0.297	0.030	ATLASgal	complex structure
251	16:54:15.3	−45:16:58	340.790	−1.009	0.030	YSO	ring or shell source
252	16:54:16.1	−45:17:31	340.785	−1.016	0.004	WISE-H II ATLASgal	ring or shell source
269	16:56:33.9	−43:46:15	342.226	−0.380	0.037	Planetary Nebula	point
290	16:59:03.9	−42:41:38	343.353	−0.066	0.032	WISE-H II ATLASgal	point
296	16:59:19.2	−42:34:17	343.478	−0.027	0.040	ATLASgal	complex structure
297	16:59:20.7	−42:32:38	343.502	−0.014	0.018	WISE-H II ATLASgal	point
305	17:00:17.1	−43:12:46	343.082	−0.562	0.084	SNR	point
319	17:02:13.1	−46:55:51	340.355	−3.114	0.129	YSO	point
322	17:02:39.5	−46:08:01	341.033	−2.687	0.114	YSO	point
331	17:04:13.1	−42:19:54	344.221	−0.594	0.029	ATLASgal	point

Table 5
Extragalactic Sources

Index	R.A.	Decl.	Longitude	Latitude	σ_τ	Structure
0	16:29:14.5	−45:41:17	337.593	+2.016	0.435	single component
1	16:29:34.5	−44:18:37	338.633	+2.922	0.190	single component
2	16:30:18.3	−44:52:32	338.312	+2.440	0.328	single component
4	16:30:34.1	−45:15:06	338.070	+2.148	0.186	single component
5	16:30:40.0	−47:00:19	336.805	+0.932	0.074	single component
6	16:30:42.7	−44:30:48	338.625	+2.635	0.164	single component
7	16:30:44.7	−44:00:14	339.001	+2.980	0.144	mean of a double source
8	16:31:13.0	−46:43:40	337.072	+1.054	0.482	single component
9	16:31:29.9	−44:28:17	338.752	+2.562	0.465	single component
10	16:31:37.9	−43:45:25	339.290	+3.032	0.036	single component
11	16:32:02.0	−46:52:53	337.055	+0.847	0.043	single component
13	16:32:38.8	−45:53:21	337.853	+1.446	0.154	single component
14	16:32:39.9	−47:34:38	336.620	+0.294	0.268	single component
15	16:32:46.7	−45:58:02	337.812	+1.376	0.024	single component
16	16:32:54.3	−43:57:00	339.306	+2.733	0.024	single component
19	16:32:57.0	−45:03:52	338.494	+1.969	0.266	single component
21	16:33:05.8	−45:09:29	338.443	+1.886	0.017	one component of a double
24	16:33:47.5	−44:09:29	339.261	+2.475	0.206	single component
25	16:33:50.7	−47:46:46	336.607	+0.011	0.103	complex structure
27	16:34:00.5	−46:19:36	337.693	+0.976	0.386	single component
28	16:34:04.0	−43:07:53	340.051	+3.134	0.161	one component of a double
38	16:35:35.5	−46:15:24	337.929	+0.822	0.344	single component
39	16:35:36.7	−43:17:37	340.122	+2.817	0.137	single component
40	16:35:48.8	−42:28:38	340.751	+3.339	0.387	single component
41	16:36:04.5	−44:57:59	338.940	+1.629	0.100	single component
42	16:36:05.4	−42:48:44	340.537	+3.076	0.259	single component
45	16:36:28.0	−46:36:47	337.767	+0.470	0.214	single component
47	16:36:30.0	−45:22:44	338.685	+1.296	0.140	single component
49	16:36:38.1	−44:45:18	339.163	+1.697	0.123	single component
53	16:36:58.0	−45:06:25	338.942	+1.418	0.050	single component
54	16:37:01.6	−43:34:02	340.091	+2.443	0.121	single component
55	16:37:04.3	−43:10:52	340.384	+2.695	0.058	single component
57	16:37:13.8	−44:23:08	339.508	+1.867	0.133	one component of a double
61	16:37:25.0	−44:10:34	339.686	+1.982	0.123	single component
62	16:37:27.9	−43:35:42	340.124	+2.365	0.128	complex structure
65	16:37:57.2	−43:01:53	340.603	+2.676	0.104	single component
70	16:38:27.3	−44:14:45	339.759	+1.797	0.043	single component
71	16:38:28.6	−45:02:19	339.171	+1.265	0.160	single component
77	16:38:59.2	−43:45:25	340.187	+2.052	0.129	single component
78	16:39:00.2	−44:50:33	339.379	+1.327	0.128	single component
80	16:39:08.7	−47:34:24	337.359	−0.511	0.463	single component
81	16:39:15.3	−46:55:04	337.861	−0.088	0.046	complex structure
84	16:39:34.6	−44:26:37	339.745	+1.516	0.052	single component
91	16:40:01.5	−44:49:14	339.516	+1.206	0.121	mean of a double source
90	16:40:01.6	−43:44:16	340.326	+1.924	0.111	single component
94	16:40:07.6	−47:02:34	337.866	−0.283	0.033	single component
95	16:40:08.9	−47:08:44	337.792	−0.354	0.228	single component
99	16:40:39.5	−43:42:35	340.423	+1.858	0.233	single component
104	16:40:57.2	−43:53:02	340.328	+1.703	0.196	single component
115	16:41:13.9	−45:12:06	339.372	+0.794	0.216	single component
117	16:41:14.9	−44:00:22	340.271	+1.582	0.081	one component of a double
120	16:41:16.0	−44:00:02	340.278	+1.583	0.037	one component of a double
123	16:41:33.0	−44:52:38	339.653	+0.966	0.225	one component of a double
127	16:41:50.5	−47:40:38	337.583	−0.920	0.035	single component
133	16:42:06.8	−44:13:33	340.209	+1.320	0.083	single component
140	16:42:39.0	−47:38:45	337.696	−1.002	0.124	single component
141	16:42:45.9	−44:00:06	340.454	+1.379	0.053	complex structure
142	16:42:46.9	−44:01:15	340.442	+1.365	0.032	complex structure
147	16:43:03.7	−46:47:23	338.387	−0.492	0.023	one component of a double
148	16:43:05.5	−44:17:38	340.273	+1.143	0.075	single component
151	16:43:18.9	−42:41:51	341.504	+2.161	0.193	single component
152	16:43:29.7	−47:10:40	338.143	−0.802	0.125	single component
153	16:43:35.5	−46:26:31	338.709	−0.332	0.187	single component
154	16:43:38.2	−45:24:14	339.498	+0.342	0.178	single component

Table 5
(Continued)

Index	R.A.	Decl.	Longitude	Latitude	σ_τ	Structure
155	16:43:47.9	−44:02:17	340.549	+1.216	0.012	single component
160	16:44:22.6	−44:36:40	340.183	+0.762	0.035	single component
159	16:44:24.2	−44:36:45	340.185	+0.758	0.051	complex structure
161	16:44:25.9	−44:19:43	340.403	+0.939	0.063	complex structure
162	16:44:28.2	−44:54:38	339.967	+0.554	0.193	single component
163	16:44:30.0	−45:41:35	339.379	+0.039	0.145	single component
164	16:44:35.6	−47:13:37	338.228	−0.975	0.157	single component
165	16:44:35.7	−47:17:23	338.180	−1.017	0.141	single component
167	16:44:48.2	−44:27:08	340.353	+0.809	0.192	single component
171	16:45:10.4	−47:32:53	338.048	−1.259	0.134	single component
172	16:45:16.0	−45:36:19	339.532	−0.006	0.138	one component of a double
173	16:45:18.6	−45:37:40	339.520	−0.026	0.032	single component
174	16:45:32.9	−47:42:34	337.967	−1.412	0.031	single component
177	16:45:49.5	−43:35:56	341.120	+1.225	0.022	single component
179	16:45:52.1	−45:18:37	339.825	+0.106	0.249	single component
181	16:46:13.7	−43:16:51	341.410	+1.376	0.075	single component
182	16:46:14.0	−44:11:53	340.713	+0.780	0.036	single component
183	16:46:22.0	−42:51:40	341.745	+1.629	0.126	single component
184	16:46:34.2	−43:39:14	341.166	+1.087	0.053	single component
185	16:46:41.3	−46:10:30	339.260	−0.564	0.255	one component of a double
186	16:46:44.5	−45:40:06	339.652	−0.242	0.014	single component
187	16:47:00.0	−46:02:31	339.397	−0.519	0.248	single component
188	16:47:00.5	−47:29:39	338.290	−1.460	0.285	single component
189	16:47:01.4	−46:49:55	338.797	−1.033	0.053	single component
192	16:47:24.0	−44:25:27	340.676	+0.474	0.155	single component
194	16:47:49.5	−43:03:13	341.771	+1.301	0.115	single component
195	16:47:50.9	−43:08:03	341.713	+1.246	0.032	mean of a double source
201	16:48:12.6	−43:02:48	341.822	+1.252	0.152	single component
203	16:48:18.0	−43:26:39	341.529	+0.983	0.162	single component
204	16:48:25.9	−46:14:33	339.404	−0.838	0.075	single component
205	16:48:30.7	−44:31:24	340.728	+0.259	0.042	single component
206	16:48:40.8	−43:33:21	341.488	+0.859	0.198	single component
207	16:48:49.1	−46:19:43	339.381	−0.944	0.086	single component
209	16:48:53.8	−47:14:34	338.689	−1.542	0.038	single component
213	16:49:23.8	−46:41:39	339.164	−1.255	0.128	single component
214	16:49:28.0	−43:14:49	341.816	+0.948	0.103	single component
216	16:49:42.7	−43:53:10	341.354	+0.504	0.023	single component
217	16:50:37.0	−46:38:42	339.336	−1.385	0.094	single component
218	16:50:38.9	−47:31:26	338.663	−1.950	0.391	single component
219	16:51:06.6	−43:08:10	342.093	+0.788	0.036	single component
221	16:51:22.5	−42:39:00	342.499	+1.061	0.140	complex structure
222	16:51:23.5	−46:50:25	339.271	−1.611	0.160	single component
223	16:51:33.9	−43:46:07	341.658	+0.322	0.042	single component
224	16:52:07.7	−47:08:21	339.120	−1.898	0.224	single component
228	16:52:29.5	−44:35:09	341.133	−0.326	0.095	one component of a double
231	16:52:34.0	−45:36:44	340.348	−0.987	0.031	single component
232	16:52:40.4	−47:28:12	338.922	−2.180	0.312	complex structure
233	16:52:45.6	−42:11:14	343.018	+1.158	0.146	single component
236	16:52:54.3	−46:37:58	339.596	−1.680	0.234	single component
237	16:53:00.2	−46:44:00	339.529	−1.756	0.038	single component
238	16:53:03.3	−46:26:17	339.763	−1.577	0.095	single component
240	16:53:18.1	−45:19:21	340.654	−0.904	0.115	single component
241	16:53:23.9	−42:45:34	342.650	+0.704	0.030	single component
242	16:53:26.1	−42:03:14	343.201	+1.145	0.030	single component
244	16:53:34.5	−42:30:40	342.863	+0.836	0.024	single component
245	16:53:39.7	−42:17:05	343.049	+0.967	0.085	single component
246	16:53:59.7	−42:20:19	343.046	+0.885	0.098	single component
247	16:54:04.1	−43:05:09	342.475	+0.403	0.032	one component of a double
249	16:54:10.7	−43:59:05	341.790	−0.180	0.175	single component
250	16:54:13.8	−47:34:37	339.005	−2.451	0.380	single component
254	16:54:29.9	−46:51:30	339.593	−2.034	0.014	single component
255	16:54:34.7	−45:24:34	340.728	−1.133	0.156	single component
256	16:54:39.8	−47:03:49	339.451	−2.185	0.093	single component
257	16:54:53.7	−45:34:16	340.637	−1.278	0.022	single component

Table 5
(Continued)

Index	R.A.	Decl.	Longitude	Latitude	σ_τ	Structure
259	16:55:05.6	−47:05:25	339.477	−2.259	0.124	single component
260	16:55:14.3	−45:33:41	340.683	−1.318	0.305	single component
261	16:55:36.3	−43:48:44	342.085	−0.271	0.050	single component
262	16:55:40.1	−46:45:25	339.798	−2.126	0.177	mean of a double source
264	16:56:01.8	−42:20:03	343.286	+0.595	0.047	single component
265	16:56:14.9	−47:29:15	339.289	−2.660	0.057	single component
266	16:56:19.9	−42:43:09	343.020	+0.311	0.201	single component
267	16:56:25.2	−43:17:05	342.589	−0.056	0.040	mean of a double source
270	16:56:36.7	−44:37:16	341.568	−0.918	0.132	one component of a double
272	16:56:58.2	−42:10:11	343.523	+0.562	0.111	complex structure
274	16:57:05.6	−44:04:02	342.054	−0.639	0.067	one component of a double
276	16:57:20.7	−45:18:22	341.113	−1.447	0.078	single component
277	16:57:27.2	−44:16:30	341.932	−0.819	0.182	single component
278	16:57:53.2	−44:02:50	342.159	−0.739	0.017	mean of a double source
280	16:57:56.4	−42:47:49	343.144	+0.032	0.096	complex structure
282	16:58:09.4	−45:19:01	341.193	−1.565	0.174	single component
283	16:58:15.0	−43:30:12	342.625	−0.452	0.063	single component
284	16:58:17.4	−47:30:51	339.483	−2.947	0.087	one component of a double
286	16:58:28.5	−42:43:38	343.259	−0.002	0.105	single component
287	16:58:31.7	−47:00:07	339.911	−2.661	0.130	single component
288	16:58:55.5	−43:54:17	342.386	−0.797	0.105	single component
289	16:59:01.1	−43:24:51	342.782	−0.506	0.019	single component
292	16:59:07.0	−42:53:03	343.209	−0.192	0.053	single component
294	16:59:08.0	−46:19:42	340.505	−2.326	0.258	single component
293	16:59:08.4	−44:39:21	341.820	−1.292	0.036	single component
295	16:59:15.1	−47:25:35	339.653	−3.020	0.261	single component
299	16:59:49.2	−44:41:48	341.863	−1.412	0.106	single component
300	16:59:54.3	−46:55:01	340.123	−2.793	0.274	single component
301	17:00:03.1	−42:28:58	343.631	−0.079	0.204	single component
302	17:00:04.8	−42:12:28	343.850	+0.087	0.058	single component
304	17:00:16.4	−42:29:41	343.646	−0.118	0.091	single component
306	17:00:30.6	−42:34:49	343.606	−0.205	0.080	mean of a double source
308	17:00:34.2	−46:57:51	340.156	−2.912	0.067	single component
309	17:00:36.5	−46:44:34	340.334	−2.781	0.218	mean of a double source
310	17:01:05.9	−42:52:28	343.440	−0.472	0.074	single component
311	17:01:08.0	−43:52:07	342.660	−1.087	0.113	one component of a double
313	17:01:13.2	−44:05:07	342.499	−1.233	0.106	single component
314	17:01:23.1	−42:46:22	343.553	−0.450	0.105	one component of a double
316	17:01:26.3	−46:39:58	340.482	−2.846	0.134	single component
317	17:01:54.0	−43:28:48	343.052	−0.958	0.353	single component
318	17:02:05.7	−47:02:28	340.254	−3.164	0.075	single component
320	17:02:21.4	−46:40:07	340.577	−2.972	0.173	single component
321	17:02:36.0	−44:55:47	341.981	−1.944	0.024	single component
323	17:02:47.5	−44:07:07	342.645	−1.476	0.013	single component
324	17:02:50.9	−45:15:51	341.743	−2.183	0.212	single component
325	17:03:03.7	−46:11:30	341.030	−2.778	0.265	single component
326	17:03:21.3	−45:50:53	341.334	−2.609	0.054	single component
327	17:03:23.8	−44:22:32	342.507	−1.719	0.201	single component
328	17:03:50.6	−45:38:21	341.552	−2.550	0.136	single component
329	17:03:54.1	−43:26:06	343.309	−1.219	0.321	one component of a double
330	17:04:10.6	−43:00:01	343.685	−0.994	0.248	single component
332	17:04:36.0	−45:13:15	341.965	−2.402	0.402	single component
333	17:04:39.3	−45:29:29	341.755	−2.573	0.378	single component
334	17:04:51.9	−45:17:20	341.939	−2.480	0.256	single component
335	17:04:53.4	−46:24:00	341.056	−3.155	0.405	one component of a double
336	17:05:07.6	−45:31:06	341.784	−2.655	0.063	mean of a double source
338	17:05:42.4	−45:41:30	341.707	−2.841	0.083	complex structure
340	17:06:20.0	−45:55:18	341.589	−3.067	0.294	single component
341	17:06:22.0	−46:00:18	341.526	−3.121	0.072	single component
342	17:06:30.2	−44:08:29	343.031	−2.020	0.261	single component
343	17:06:57.9	−45:37:09	341.897	−2.973	0.078	complex structure
346	17:07:48.6	−46:00:42	341.671	−3.326	0.492	single component

ORCID iDs

John M. Dickey https://orcid.org/0000-0002-6300-7459
J. M. Dempsey https://orcid.org/0000-0002-4899-4169
N. M. Pingel https://orcid.org/0000-0001-9504-7386
N. M. McClure-Griffiths https://orcid.org/0000-0003-2730-957X
K. Jameson https://orcid.org/0000-0001-7105-0994
J. R. Dawson https://orcid.org/0000-0003-0235-3347
H. Dénes https://orcid.org/0000-0002-9214-8613
S. E. Clark https://orcid.org/0000-0002-7633-3376
D. Leahy https://orcid.org/0000-0002-4814-958X
Min-Young Lee https://orcid.org/0000-0002-9888-0784
M.-A. Miville-Deschênes https://orcid.org/0000-0002-7351-6062
S. Stanimirović https://orcid.org/0000-0002-3418-7817
C. D. Tremblay https://orcid.org/0000-0002-4409-3515
J. Th. van Loon https://orcid.org/0000-0002-1272-3017

References

Allison, J. R. 2021, MNRAS, 503, 985
Anderson, L. D., Armentrout, W. P., Johnstone, B. M., et al. 2015, ApJS, 221, 26
Banda-Barragán, W. E., Brüggen, M., Federrath, C., et al. 2020, MNRAS, 499, 2173
Benjamin, R. A. 2008, in ASP Conf. Ser. 387, Massive Star Formation: Observations Confront Theory, ed. H. Beuther, H. Linz, & Th. Henning (San Francisco, CA: ASP), 375
HI4PI Collaboration, Ben Bekhti, N., Flöer, L., et al. 2016, A&A, 594, A116
Bialy, S., Neufeld, D., Wolfire, M., Sternberg, A., & Burkhart, B. 2019, ApJ, 885, 109
Bland-Hawthorn, J., & Gerhard, O. 2016, ARA&A, 54, 529
Bland-Hawthorn, J., Maloney, P. R., Stephens, A., Zovaro, A., & Popping, A. 2017, ApJ, 849, 51
Brand, J., & Blitz, L. 1993, A&A, 275, 67
Chippendale, A. P., O'Sullivan, J., Reynolds, J., et al. 2010, in IEEE Int. Symp. on Phased Array Systems and Technology (Piscataway, NJ: IEEE), 648
Chippendale, A. P., Beresford, R. J., Deng, X., et al. 2016, in Int. Conf. Electromagn. Adv. Appl. (Piscataway, NJ: IEEE), 909
Chrobáková, Z. ˇ, Nagy, R., & López-Corredoira, M. 2020, A&A, 637, A96
Churchwell, E., Povich, M. S., Allen, D., et al. 2006, ApJ, 649, 759
Churchwell, E., Babler, B. L., Meade, M. R., et al. 2009, PASP, 121, 213
Clark, B. G. 1965, ApJ, 142, 1398
Davies, R. D., & Cummings, E. R. 1975, MNRAS, 170, 95
Das, S., Sardone, A., Leroy, A. K., et al. 2020, ApJ, 898, 15
Dempsey, J., McClure-Griffiths, N. M., Jameson, K., & Buckland-Willis, F. 2020, MNRAS, 496, 913
Dempsey, J., Murray, C., McClure-Griffiths, N. M., et al. 2021, PASA, submitted
Dickey, J. M., & Lockman, F. J. 1990, ARA&A, 28, 215
Dickey, J. M., McClure-Griffiths, N. M., Gaensler, B. M., & Green, A. J. 2003, ApJ, 585, 801
Dickey, J. M., Strasser, S. T., Gaensler, B. M., et al. 2009, ApJ, 693, 1250
Dickey, J. M., McClure-Griffiths, N., Gibson, S. J., et al. 2013, PASA, 30, e003
Draine, B. T. 2011, Physics of the Interstellar and Intergalactic Medium (Princeton, NJ: Princeton Univ. Press)
Dutta, A., Sharma, P., & Nelson, D. 2022, MNRAS, 510, 3561
Ferrière, K. M. 2001, RvMP, 73, 1031
Field, G. B., Goldsmith, D. W., & Habing, H. J. 1969, ApJL, 155, L149
Fox, A. J., Wakker, B. P., Barger, K. A., et al. 2014, ApJ, 787, 147
Gazol, A., & Villagran, M. A. 2016, MNRAS, 462, 2033
Gordon, M. A. 1976, in Methods of Experimental Physics, Vol. 12: Astrophysics, Part C: Radio Observations, ed. M. L. Meeks (New York: Academic), 277
Green, D. A. 2019, JApA, 40, 36
Guzman, J., Whiting, M., Voronkov, M., et al. 2019, ascl:1912.003
Haverkorn, M., Gaensler, B. M., McClure-Griffiths, N. M., Dickey, J. M., & Green, A. J. 2006, ApJS, 167, 230
Heiles, C., & Troland, T. H. 2003, ApJ, 586, 1067
Hotan, A. W., Bunton, J. D., Chippendale, A. P., et al. 2021, PASA, 38, e009
Hunter, J. D. 2007, CSE, 9, 90
Jameson, K. E., McClure-Griffiths, N. M., Liu, B., et al. 2019, ApJS, 244, 7
Kalberla, P. M. W., Burton, W. B., Hartmann, D., et al. 2005, A&A, 440, 775
Kalberla, P. M. W., & Dedes, L. 2008, A&A, 487, 951
Kalberla, P. M. W., & Kerp, J. 2009, ARA&A, 47, 27
Kalberla, P. M. W., McClure-Griffiths, N. M., Pisano, D. J., et al. 2010, A&A, 521, A17
Kanekar, N. 2014, ApJL, 797, L20
Kanekar, N., Prochaska, J. X., Smette, A., et al. 2014, MNRAS, 438, 2131
Koo, B.-C., Park, G., Kim, W0T., et al. 2017, PASP, 129, 094102
Kulkarni, S. R., & Heiles, C. 1987, in Astrophys. Space Sci. Libr. 134, Interstellar Processes, ed. D. J. Hollenbach & H. A. Thronson (Dordrecht: Reidel), 87
Liszt, H. S. 2001, A&A, 371, 698
Liszt, H. S. 2002, A&A, 389, 393
Lockman, F. J. 1984, ApJ, 283, 90
Lockman, F. J., & Gehman, C. S. 1991, ApJ, 382, 182
Malhotra, S. 1995, ApJ, 448, 138
Manchester, R. N., Hobbs, G. B., Teoh, A., & Hobbs, M. 2005, AJ, 129, 1993
Martin, C. L., Ho, S. H., Kacprzak, G. G., & Churchill, C. W. 2019, ApJ, 878, 84
McClure-Griffiths, N. M., Dickey, J. M., Gaensler, B. M., et al. 2005, ApJS, 158, 178
McClure-Griffiths, N. M., Pisano, D. J., Calabretta, M. R., et al. 2009, ApJS, 181, 398
McClure-Griffiths, N. M., & Dickey, J. M. 2016, ApJ, 831, 124
Miller, M. J., & Bregman, J. N. 2015, ApJ, 800, 14
Miville-Deschênes, M.-A., Murray, N., & Lee, E. J. 2017, ApJ, 834, 57
Murray, C. E., Stanimirović, S., Goss, W. M., et al. 2015, ApJ, 804, 89
Murray, C. E., Stanimirović, S., Goss, W. M., et al. 2018, ApJS, 238, 14
Murray, C. E., Peek, J. E. G., & Kim, C.-G. 2020, ApJ, 899, 15
Murray, C. E., Stanimirović, S., Heiles, C., et al. 2021, ApJS, 256, 37
Nelson, D., Sharma, P., Pillepich, A., et al. 2020, MNRAS, 498, 2391
Nguyen, H., Dawson, J. R., Lee, M.-Y., et al. 2019, ApJ, 880, 141
Nuza, S. E., Scannapieco, C., Chiappini, C., et al. 2019, MNRAS, 482, 3089
Pingel, N. M., Pisano, D. J., Heald, G., et al. 2018, ApJ, 865, 36
Pingel, N. M., Dempsey, J., McClure-Griffiths, N. M., et al. 2022, PASA, 39, e005
Pisano, D. J. 2014, AJ, 147, 48
Preite-Martinez, A. 1988, A&AS, 76, 317
Putman, M. E., Peek, J. E. G., & Joung, M. R. 2012, ARA&A, 50, 491
Radhakrishnan, V., Goss, W. M., Murray, J. D., & Brooks, J. W. 1972, ApJS, 24, 49
Reid, M. J., Menten, K. M., Brunthaler, A., et al. 2014, ApJ, 783, 130
Reid, M. J., Menten, K. M., Brunthaler, et al. 2019, ApJ, 885, 131
Riggi, S., Umana, G., Trigilio, C., et al. 2021, MNRAS, 502, 60
Sardone, A., Pisano, D. J., Pingel, N. M., et al. 2021, ApJ, 910, 69
Seon, K.-I., & Kim, C-G. 2020, ApJS, 250, 9
Stanimirović, S., Murray, C. E., Lee, M.-Y., Heiles, C., & Miller, J. 2014, ApJ, 793, 132
Stewart, K. R., Kaufmann, T., Bullock, J. S., et al. 2011, ApJ, 738, 39
Strasser, S. T. 2006, PhDT, University of Minnesota: Minneapolis
Strasser, S. T., Dickey, J. M., Taylor, A. R., et al. 2007, AJ, 134, 2252
Su, Y., Yang, J., Yan, Q.-Z., et al. 2021, ApJ, 910, 131
Trapp, C. W., Kereš, D., Chan, T. K., et al. 2022, MNRAS, 509, 4149
Tumlinson, J., Peeples, M. S., & Werk, J. K. 2017, ARA&A, 55, 389
Urquhart, J. S., Csengeri, T., Wyrowski, F., et al. 2014, A&A, 568, A41
Vallée, J. P. 2020, ApJ, 896, 19
Vázquez-Semadeni, E., Ryu, D., Passot, T., Gonzáles, R. F., & Gazol, A. 2006, ApJ, 643, 245
Wegg, C., Gerhard, O., & Portail, M. 2015, MNRAS, 450, 4050
Wenger, T. V., Balser, D. S., Anderson, L. D., & Bania, T. M. 2018, ApJ, 856, 52
Wenger, T. V., Balser, D. S., Anderson, L. D., & Bania, T. M. 2019, ApJ, 887, 114
Whiting, M., & Humphreys, B. 2012, PASA, 29, 371
Wolfire, M. G., Hollenbach, D., McKee, C. F., Tielens, A. G. G. M., & Bakes, E. L. O. 2003, ApJ, 443, 152
Wolfire, M. G., McKee, C. F., Hollenbach, D., & Tielens, A. G. G. M. 2003, ApJ, 587, 278